

Deformation Behavior of adidas BOOST™ Foams Using *In Situ* X-ray Tomography and
Correlative Microscopy

by

Arun Sundar Sundaram Singaravelu

A Dissertation Presented in Partial Fulfillment
of the Requirements for the Degree
Doctor of Philosophy

Approved June 2020 by the
Graduate Supervisory Committee:

Nikhilesh Chawla, Chair
Heather Emady
Yang Jiao

ARIZONA STATE UNIVERSITY

August 2020

ABSTRACT

Energy return in footwear is associated with the damping behavior of midsole foams, which stems from the combination of cellular structure and polymeric material behavior. Recently, traditional ethyl vinyl acetate (EVA) foams have been replaced by BOOST™ foams, thereby reducing the energetic cost of running. These are bead foams made from expanded thermoplastic polyurethane (eTPU), which have a multi-scale structure consisting of fused porous beads, at the meso-scale, and thousands of small closed cells within the beads at the micro-scale. Existing predictive models coarsely describe the macroscopic behavior but do not take into account strain localizations and microstructural heterogeneities. Thus, enhancement in material performance and optimization requires a comprehensive understanding of the foam's cellular structure at all length scales and its influence on mechanical response.

This dissertation focused on characterization and deformation behavior of eTPU bead foams with a unique graded cell structure at the micro and meso-scale. The evolution of the foam structure during compression was studied using a combination of *in situ* lab scale and synchrotron x-ray tomography using a four-dimensional (4D, deformation + time) approach. A digital volume correlation (DVC) method was developed to elucidate the role of cell structure on local deformation mechanisms. The overall mechanical response was also studied *ex situ* to probe the effect of cell size distribution on the force-deflection behavior. The radial variation in porosity and ligament thickness profoundly influenced the global mechanical behavior. The correlation of changes in void size and shape helped in identifying potentially weak regions in the microstructure. Strain maps showed the initiation of failure in cell structure and it was found to be influenced by the heterogeneities

around the immediate neighbors in a cluster of voids. Poisson's ratio evaluated from DVC was related to the microstructure of the bead foams. The 4D approach taken here provided an in depth and mechanistic understanding of the material behavior, both at the bead and plate levels, that will be invaluable in designing the next generation of high-performance footwear.

*To my parents and my sister for
encouraging and supporting me in everything and
for teaching me to work hard for what I want.*

ACKNOWLEDGMENTS

I would like to express my sincere gratitude and thanks to my advisor, Professor Nikhilesh Chawla for providing continuous guidance and encouragement to support me in conducting successful research. I would also like to thank my committee members Dr. Yang Jiao and Dr. Heather Emady for taking time to evaluate my doctoral research. I would like to acknowledge the financial support from adidas. Specifically, I would like to thank our collaborators at adidas, Jasmin Ruppert, Maxmilian Drexler, Mark Henderson and Chris Holmes.

I would like to acknowledge the use of facilities within the Center for 4D Materials Science (4DMS) and Keck Division of College of Liberal Arts and Sciences (CLAS) at ASU. I would also like to thank Dr. F. De Carlo and Pavel D. Shevchenko at Argonne National Laboratory for assistance with x-ray synchrotron tomography to perform this work. Use of the Advanced Photon Source (APS) was supported by the U.S. Department of Energy, Office of Science, Office of Basic Energy Sciences, under Contract No. DE-AC02-06CH11357.

In addition, I would like to thank and acknowledge the advice of Research Scientist, Dr. Jason Williams at various stages during my research work. I would also like to thank all my colleagues in Professor Chawla's Research Group, former and current, for their help and collaboration. A special thanks to Antony and Sridhar for their support.

Finally, my special thanks go to my family and friends in India and Tempe for their support, patience and encouragement throughout the course of this Ph.D. research. Thanks to

Prasanna and Anjana for having supported me through everything. Thanks to Ksjusha for her help. Thanks to Dr. V Anbazhagan for sharing his views and introducing me to fellow metallurgists. And last, I would like to extend my deepest gratitude to my parents and my sister for their love, sacrifice, patience, and for making me the person I am today.

TABLE OF CONTENTS

	Page
LIST OF TABLES	viii
LIST OF FIGURES	ix
CHAPTER	
1 INTRODUCTION	1
2 LITERATURE REVIEW	4
2.1 Thermoplastic Polyurethane.....	4
2.2 Bead Foams	5
2.3 Mechanical Behavior of Bead Foams.....	10
2.4 Digital Volume Correlation.....	16
2.5 Research Objectives	17
3 <i>IN SITU</i> X-RAY MICROTOMOGRAPHY OF THE COMPRESSION BEHAVIOR OF eTPU BEAD FOAMS WITH A UNIQUE GRADED STRUCTURE	19
3.1 Introduction.....	19
3.2 Materials and Methods	21
3.2.1 General Overview of Testing	21
3.2.2 Interrupted <i>in situ</i> CT	23
3.2.3 Image Analysis	24
3.3 Results and Discussion.....	25
3.3.1 Morphological Characteristics	25
3.3.2 Structural Changes during Compression	31

CHAPTER	Page
3.3.3 Local Deformation Inhomogeneities with Aid of Strain Maps.....	40
3.3.3.1 Local Strain Distribution by DVC	41
3.3.3.1 Local Void Collapse and Deformation Instabilities	46
3.4 Conclusions.....	51
4 MECHANISMS OF DEFORMATION IN ϵ TPU MOLDED BEAD FOAMS IN COMPRESSION VIA <i>IN SITU</i> SYNCHROTRON X-RAY MICROTOMOGRAPHY	52
4.1 Introduction.....	52
4.2 Materials and Methods	54
4.2.1 General Overview of Testing	54
4.2.2 <i>In situ</i> Microtomography at the Advanced Photon Source (APS).....	56
4.2.3 Image Analysis	59
4.2.4 Estimating Strains using DVC	63
4.3 Results.....	64
4.3.1 Morphological Characteristics	64
4.3.2 Poisson Ratio	71
4.4 Discussion.....	74
4.5 Conclusion	78
5 CONCLUSIONS	79
5.1 Summary of Research Findings	79
5.2 Future Work.....	80
REFERENCES	81

LIST OF TABLES

Table	Page
1. Total Applied Strain and Local Strain Values of Different Beads in the 2D Tomographic Slice Analysis for Several Impacts [11].	14
2. Details of the X-ray Scans of Different Samples Along With Their Strain State During Imaging. LR and HR Denotes Low-Resolution and High-Resolution Scan Respectively.	22
3. Details of the Void Size and Ligament Thickness Distributions Shown in Figure 28.	70

LIST OF FIGURES

Figure	Page
1. Photograph of the Molded Foam Beads With Hundreds of Individual Beads Which are Themselves Composed of Microcells (From Left to Right).	1
2. Schematic Representation of a Segmented TPU [20].	5
3. Schematic of (a) Autoclave Batch Process and (b) Extrusion Process Used for Manufacturing TPU beads. Adapted From Ref. [34].	7
4. A Typical Double-Peak Melting Behavior of the Foamed Beads.	9
5. Structural Features of Bead Foams (From Polymer Taken as an Example) at Different Spatial Scales. Illustration Images at the Nano-Scale are Adapted from Ref.[21].	11
6. (a) Experimental Setup of Compression in the Lab Scale CT System With the Loading Fixture. Inset Shows the Top and Bottom Platens at a Higher Magnification. (b) Schematic of the Loading Fixture.	22
7. SEM Image of the Cryo-Sectioned Bead Foam Surface Showing the Variation in Void Size and Ligament Thicknesses From the Surface to Core of the Bead. (a) Low Magnification View Showing Half the Bead. (b) and (c) High Magnification Images of the Regions Within the Red (Close to Surface) and Orange (Transition Area) Boxes in (a).	24
8. Image Analysis Workflow With the Different Steps During the Process. (a) Grayscale Image, (b) Filtered Image, (c) Thresholded Image, (d) Dilated Image, (e) Eroded Image and (f) Border Killed Image.	25

Figure	Page
9. X-ray CT Slice From the Mid-Section of Sample Before Compression at Zero Strain Showing the Heterogeneity in Cell Structure. (a) Slice From LR Scan of Whole Bead Along Compression Direction. (b) Slice From HR Scan of the Region Within the Dashed Orange Box (Close to the Bottom of the Image) in (a). (c) and (d) Slice in the XZ and YZ axis, Which are Orthogonal to (a). The Compression Axis is Along the X Axis.	28
10. (a) 3D Rendering of the Foamed Bead, (b) 3D Rendering of the Compression of Foamed Bead With the Coordinate System Used Throughout This Chapter.	28
11. Plot of Void Position Against its Diameter Showing the Variation in Size From Surface to Core of the Sample Along the Compression Axis (X) and Orthogonal to it (Y). a, b and c are Data Along Compression of Sample A, B and C. d, e and f are Data Along Orthogonal Direction to Compression of Sample A, B and C. Open Symbols Represent Data from HR Scans, While Filled Symbols Represent Data from LR Scans. Dashed Arrow Indicates the Centre of the Sample Along Compression Axis. Hypothetical Distribution is Shown as the Region Bound Within the Triangle in c and f.	30
12. Grayscale Volume Rendering of the Bead Taken at (a) 0% Strain and (b) 50% Strain Showing the External Shape Change. The Platens are Shown as a Thin Disc for Clarity.	32
13. (a-f) Grayscale Image of Mid-Section of Sample C Under Compression in Multiples of 10% Strain Increments From 0 to 50% Strain. The Top and Bottom Platens are Marked on One End for Clarity.	35

Figure	Page
14. Plot Showing the Change in Volume of Voids in Sample C at Different Position Along the Compression Axis at 10% and 25% Applied Strain. The Centre Along this Axis is Marked by a Dashed Arrow.	36
15. Grayscale Image Close to the Free Surface of the Bead Under Compression at (a) 0% and (b) 50% Strain. ROI Shown is Marked With Dashed Blue Line in Fig.9.a. Compression Axis is in the Plane of the Figure, Top-Down.	37
16. (a-f) Grayscale Image of Same Section From the HR Scan of Sample C Near Bottom Platen in Increments of 5% Applied Strain From 0 to 25%. Bottom Platen is Noticeable Only in (a) and (f). Compression Direction is In-Plane to the Figure (Top-Down). White Arrow Points to Pre-Buckled Ligament. Red and Yellow Arrow Points to Cell-Walls of Void C Having Different Initial Curvature.	40
17. (a) Visualization of the Voids Used as Markers in DVC and (b) Volume Bounds Encompassing the Voids for Calculation of Displacement Field. Void Colouring is Random and is Unconnected. Void Renderings are From the HR Scan of Sample C at Zero Strain. Foam Structure is Shown Semi-Transparent in (a).	42
18. (a) - (d) Schematic of DVC Routine With Help of 2D Visualization.	43
19. (a) Strain Along Loading Direction (ϵ_{xx}) in a Bead Foam Under Compression Computed From DVC. (b) Strain Field of Region Near Platen Marked in (a). (c) Plot Showing the Correlation Between the Externally Applied Strain Against the Measured Strain Along the Compression Direction Using DVC in Different Regions.	45

Figure	Page
20. (a) Plot Showing the Changes in Volume of Four Adjacent Voids in Increments of 5% Strain. Position of the Void From the Contact Surface and its Size is Also Specified. (b) 3D Rendering of the Group of Voids at Multiple Strain Levels. Data and Snapshot are of the Marked-Up Voids in Figure 16 (a). Void A is not Rendered for Clarity. Regions Within the Dotted Circles Correspond to Variation in Cell-Wall Curvature and Pre-Buckled Ligaments. White, Red and Yellow Arrows Point to Same Features Marked in Figure 16 (a).....	48
21. Strain Maps (ϵ_{xx} , ϵ_{yy}) of the ROI in Fig.16 at an Applied Strain of (a)-(b) 5% and (c)-(d) 15%. Units of Strain is Percentage. Positive and Negative Values Denote Compression and Tension. Strain in the Ligaments and Voids are Shown Separately for Clarity. White, Red and Yellow Arrows Point to Same Features in Figure 16 (a) and Figure 20 (b).....	50
22. (a) Photographs of the Samples Used for Testing, i.e., Individual Beads and Molded Plate Samples. Scanning Electron Microscope Image of (b) Molded Plate Showing Multiple Bead Interfaces and the Cell Structure Within Beads and (c) High Magnification Image of the Interface.....	56
23. (a) Schematic of Beamline and Loading Fixture Layout for CT Imaging With the <i>In Situ</i> Compression Testing. (b) Plot of Applied Strain Versus Time Showing the Continuous Straining and Intermittent Scans During Which the Motor Y is Programmed to Move to Allow Vertical Sitched Scans.	59

Figure	Page
24. Flowchart of the Process Used in Image Segmentation, i.e., Labelling Voids. Process Involves Smoothing the Data, Isolating Voids, and an Iterative Selection of Voids Based on Size Criterion.	61
25. (a) Grayscale Image of Molded Plate at Zero Strain From CT. (b) Labelled Image of the Same Slice Shown in (a) After Image Segmentation Using Algorithm in Figure 24. (c) Labelled Image of the Same Slice Shown in (a) After Conventional Thresholding. (d) Grayscale Values of the Lines Marked in (a) Showing the Intensity Variation Between Voids and Ligaments. (e) Plot of Voids Identified and Labelled at Every Iteration for Three Strain Levels Plus Zero Strain With Final Count Indicated Against Strain State.	63
26. X-ray CT Slice of Samples Before Compression at Zero Strain. (a) and (b) Individual Beads With Graded Cell Structure. (c) and (d) Molded Plates From Graded Beads. (e) and (f) Individuals Beads With Graded Cell Structure Compressed Using Lab Scale CT. ROI in (f) is Limited to Region Near the Platen. BG- Bead Graded, PG-Plate Graded, BG-h-Bead Graded High Resolution. Dashed Circle Represents the Largest Ligament Size.	66
27. X-ray CT Slice of Samples at Zero Strain With Homogeneous Cellular Structure. (a) Individual Bead. (b) Molded plate. BH – Bead Homogeneous, PH – Plate Homogeneous.	67

Figure	Page
28. Relative Frequency Distributions of the Ligament Thickness (a, c, e) and Void Equivalent Diameter (b, d, f) of the Samples. (a) and (b) are for Individuals Beads With Graded Cell Structure (BG). (c) and (d) are for Molded Plates from Graded Beads (PG).	69
29. X-ray CT Slice of Molded Plate Samples Before Compression and at an Applied Compressive Strain of 22%. a and c Zero Strain. b and d 22% Strain. PG – Plate Graded, PH – Plate Homogeneous.....	71
30. Plot Showing the Variation in Volumetric Strain Against the Compressive Strain of the Bead Foam Samples. (a) Graded Individual Beads and Molded Plates From Graded Beads. (b) Molded Plates From Homogeneous and Graded Beads. Symbols Indicate Experimental Data from DVC. Solid Lines Represent Poisson Ratio Calculated Based on Eq. (9).....	73
31. Schematic of Springs Connected in Series Used to Explain the Variation in Strains due to Varying Ligament Thickness in Foams.	76
32. X-ray CT Slice of Bead Samples at an Applied Compressive Strain of 28%. (a) BG-1 (b) BG-2.	77

CHAPTER 1

INTRODUCTION

Polymeric foams are common, finding applications in automotive, aerospace, construction and sporting industries. Their unique physical, mechanical, thermal and acoustic properties are linked to its cellular structure. Bead foams are one type of foam, composed of fused beads (in the size range of millimeters) which themselves are made of microcells as shown in Figure 1.



Figure 1: Photograph of the molded foam beads with hundreds of individual beads which are themselves composed of microcells (from left to right).

In the present work, bead foams made from thermoplastic polyurethane (TPU) used in midsoles of running shoes are of interest. In the last two decades, there has been a large volume of research focusing on new materials and their optimization for production of bead foams [1–7]. With the new bead foams, the additional focus of the investigation has been in processing these bead foams to achieve good fusion in the final molded part [8–10]. Depending on the base polymer, foaming technique, and the local foam density, the mechanical properties vary widely. In addition, the loading direction, strain rate,

temperature, time-dependent material behavior complicates the mechanistic understanding of the material behavior.

The mechanical behavior of bead foams has been studied through a variety of macro-scale mechanical testing methods [11–13]. These techniques range from simple compression testing, on commercially available machines to high strain testing in a fluidized chamber, which require sophisticated experimental design and execution. Since it is imperative to obtain a complete understanding of the deformation mechanism to establish structure-property relationships, testing is usually carried out under various kinds of mechanical loads [14–16]. Special importance has been given to *in situ* studies, which provide real time deformation information using X-ray tomography [17, 18]. These studies give 3D visualization of the whole sample volume along with the influence of micro- and mesoscopic structures on the macroscopic behavior. A majority of the work done to date has focused on expanded polypropylene (EPP) and expanded polystyrene (EPS) foams having foamed beads with a uniform cell structure. Their strengthening as well as deformation mechanisms are well established from the quasi-static to dynamic strain rates. However, such extensive work has not been done on expanded thermoplastic polyurethane (eTPU) bead foams. The unique gradation in the cellular structure in the foams studied in our work (see Figure 1) and the morphological variations in these bead foams makes the understanding of material behavior and validation of existing predictive models more complex. Thus, there is a great need to understand how a particle's cellular microstructure influences the mechanical properties during compression.

This work is aimed at creating a better understanding of the influence of cell structure of bead foams. It answers some very important questions for bead foams that have not been previously investigated. The deformation behavior of these eTPU bead foams was studied through 4D (deformation + time) X-ray microtomography. The mechanical response to the applied strain evaluated through *in situ* compression in an interrupted and continuous fashion. Further, the morphological variation in the eTPU bead foams have been characterized. A digital volume correlation method has been developed to elucidate the role of cell structure on the deformation mechanism and fundamental material constant. The mechanical response was also studied *ex situ* to probe into the effect of cell size distribution present in the microstructure on the force-deflection curves. In addition, an eTPU bead foam having homogeneous cellular structure was also studied. The mechanical properties of these bead foams were evaluated and correlated with the cellular structure at the micro-scale.

CHAPTER 2

LITERATURE REVIEW

2.1 Thermoplastic Polyurethane

Thermoplastic polyurethanes (TPU) are an important class of polymeric materials that combine the mechanical properties of elastomers with the processability of thermoplastic polymers. They present remarkable properties such as good abrasion resistance, low temperature flexibility, a wide range of mechanical strength and toughness and low compression set [1, 19]. TPU elastomers are multi-block copolymers comprised of alternating soft and hard segments chemically linked together along a macromolecular backbone as schematically shown in Figure 2. The soft segment (SS) usually has their glass transition temperature (T_g) well below the service or ambient temperature and provides the spring-like elasticity to the elastomer. The hard segment (HS) has a T_g or crystalline melting temperature (T_m) above the service temperature range and behaves as a multifunctional tie point functioning both as a physical crosslink and reinforcing filler that controls mechanical properties. At the working temperature, thermodynamic immiscibility of the hard and soft segments results in phase separation and consequently a micro-domain structure of HS domains dispersed in the SS matrix is formed [20, 21]. Such a structure was first proposed by Cooper and Tobolsky and is responsible for the peculiar properties of TPUs [22, 23].

Using an Avrami analysis, Begenir et al. [24] studied the isothermal crystallization kinetics of TPU with different HS concentrations. From the Avrami exponent values and morphological observations they concluded that crystallization (hard segments) in TPUs

takes place in three dimensions from pre-existing nuclei. The crystals grow under isothermal conditions and drive the microphase separation of crystalline and amorphous regions. These HS crystallites in the microstructure can also act as heterogenous bubble nucleation sites during foaming and can be used for controlling the microstructure of foams [21, 23]. TPU structures and properties change as a function of temperature and these changes have been extensively investigated by several techniques such as differential scanning calorimetry [25–27], small and wide-angle X-ray scattering [28–30] and dynamic mechanical analysis [22, 31].

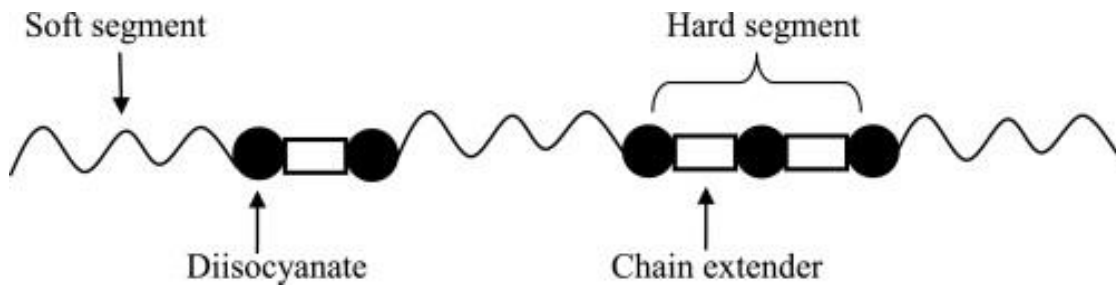
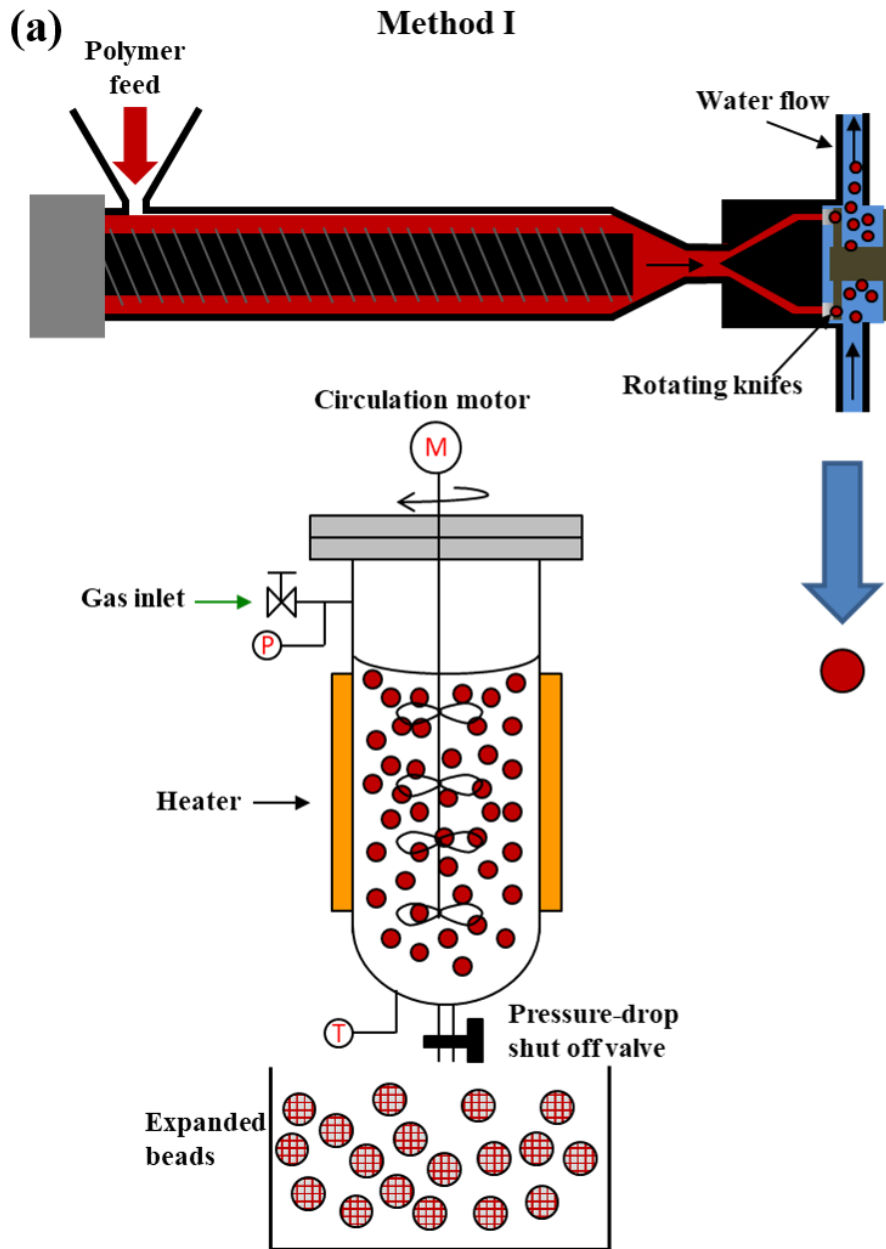


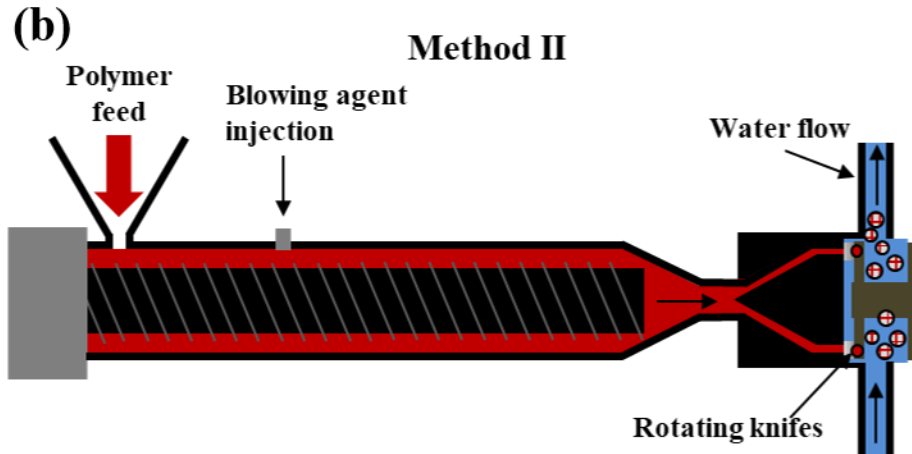
Figure 2: Schematic representation of a segmented TPU [20].


2.2. Bead Foams

For years, injection molding and extrusion have been the two major technologies used for manufacturing recyclable thermoplastic foams. With extrusion foaming, simple geometries with large volume expansion ratios and densities can be fabricated, whereas thin walled complex shapes are made using injection molding. In recent times, bead foams have received a lot of attention due to their ease in filling intricate shapes and well as their relatively low density which cannot be achieved using conventional foams [1, 3]. Established base polymers in the market for preparation of bead foams are polystyrene, polyethylene, and polypropylene. Bead foams are currently used as packaging materials,

bumper cores in the automotive field, in cushioning products, and as midsoles in shoes [1, 2, 10, 32]. Some of the new candidate materials are thermoplastic polyurethane (beneficial properties of elastomers and thermoplastics), polyactide acid (biodegradable), polybutylene terephthalate (used at temperatures up to 150°C) and polyether block amide [1, 33].





 **Micro granules (unfoamed)**

 **Foamed bead**

**Method I – Extrusion with Underwater granulation
+ Autoclave foaming**

**Method II – Extrusion with blowing agent combined
with Underwater Granulation and foaming**

Figure 3: Schematic of (a) autoclave batch process and (b) extrusion process used for manufacturing TPU beads. Adapted from Ref. [34].

Bead foam processing has two main steps: bead fabrication and bead molding. The bead fabrication either creates an initial bead which must then be expanded, or there is a direct creation of expanded beads. The final parts made are comprised of small foamed particles which are fused together. An overview of the autoclave-based process (Method I)

and extrusion method (Method II) to obtain expanded beads is shown in Figure 3. In method I, unfoamed microgranules with the required additives are granulated from an extrusion line and fed into a pressure vessel or autoclave filled with a liquid. The suspended microgranules are impregnated with a blowing agent around its melting temperature to saturation. Foaming is initiated by the sudden drop in pressure by opening the valve at the bottom of the autoclave. A good description of the influence of processing parameters in a lab scale autoclave system on the cellular morphology and crystallization behavior can be found in the work of Guo et al.[3], Zhao et al.[35] and others [21, 33]. In method II, the polymer is mixed in an extruder (either a single screw/twin screw, tandem setup) to a molten state along with the blowing agent (introduced in the system). The gas-loaded melt is then extruded through a perforated plate and cut by rotating knives in water. The pressure of the water flow is kept below that of the vapor pressure of the blowing agent to allow foaming and, thus, expandable beads. The effect of processing parameters on the shape and morphology of the beads can be found in the work of Koppl et al. [4].

The commercialized method for processing foamed beads to a finished part is done through steam chest molding, wherein steam functions as a heating medium to induce interbead bonding [10]. The working mechanism of steam chest molding is similar to that of a sintering process. High temperature steam is injected into the mold in multiple cycles to soften and fuse the beads. The steam vaporizes the volatile gas present in the beads causing an expansion in volume, as well as re-blowing of the beads. Through this process, the empty space is filled and at the same time inter-bead fusion is created [8]. This fusion is made possible by the unique melting characteristic of foamed beads shown in Figure 4. The dual peaks are attributed to the variations in polymer crystallinity resulting from

orientation of polymer chains during the bead foaming process. The hatched area in Figure 4. represents the desirable steam temperature range for the steam-chest processing, located between the high and low melting peaks. The unmelted high melting temperature (T_{m-high}) crystals help maintain the overall cell structure, while the low melting temperature (T_{m-low}) crystals melt and aid the surface fusion and sintering of individual beads [3, 10]. The formation mechanism for inter-bead bonding in steam chest processing has been proposed by several researchers [8, 10, 36]. They believed that the steam heating softened the bead foam surface, which allowed inter-diffusion of polymer chains between the beads. Subsequently physical entanglement of the chains with or without recrystallization occurs based on the type of polymer. The inter-bead bonding strength determines the mechanical properties of the molded bead foam product, because the fracture path usually forms and develops in the inter-bead bonding regions [5, 8, 9]. A good description of the influence of steam chest processing parameters on the surface properties and thermal properties can be found in the work of Hossieny et al. [9] and Zhao et al. [35].

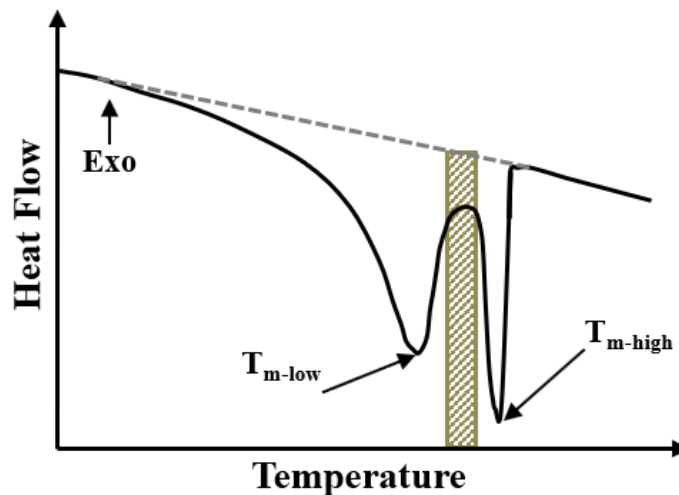


Figure 4: A typical double-peak melting behavior of the foamed beads.

2.3. Mechanical Behavior of Bead Foams

The macroscopic mechanical behavior of traditional cellular materials has been well studied. Under static or dynamic compressions, the foam response exhibits three regimes: (a) elastic behaviour, (b) by a stress plateau corresponding to plastic yielding, and (c) at higher strains, a rising hardening region corresponding to foam densification [37–39]. Like any other cellular material, the mechanical behavior of bead foams should also be dependent on the characteristics and properties at different spatial scales. At least four spatial scales can be distinguished in bead foams, as shown in Figure 5. At the macro-scale, the bead foams are characterized by the overall geometry and physical properties. The length scale ($>10^{-1}$ m) here varies based on the testing methodology, i.e., either a whole component or a test coupon with several fused beads. The spatial scale at which the individual foamed beads are arranged and connected in space is defined as the meso-scale (10^{-1} to 10^{-4} m). Further down in length scale, the individual cells within the foamed beads, interface region between neighboring beads and constituent base material covers the micro-scale (10^{-4} to 10^{-6} m). The orientation, arrangement and fraction of hard/soft segments of polymer chains, porosities and additives which influence/alter the base polymer/foaming covers the nanoscale ($<10^{-6}$) behavior. A thorough fundamental understanding of the mechanisms at different length scales in bead foams, under various loading conditions will enable designing the optimal structure required for a desired application.

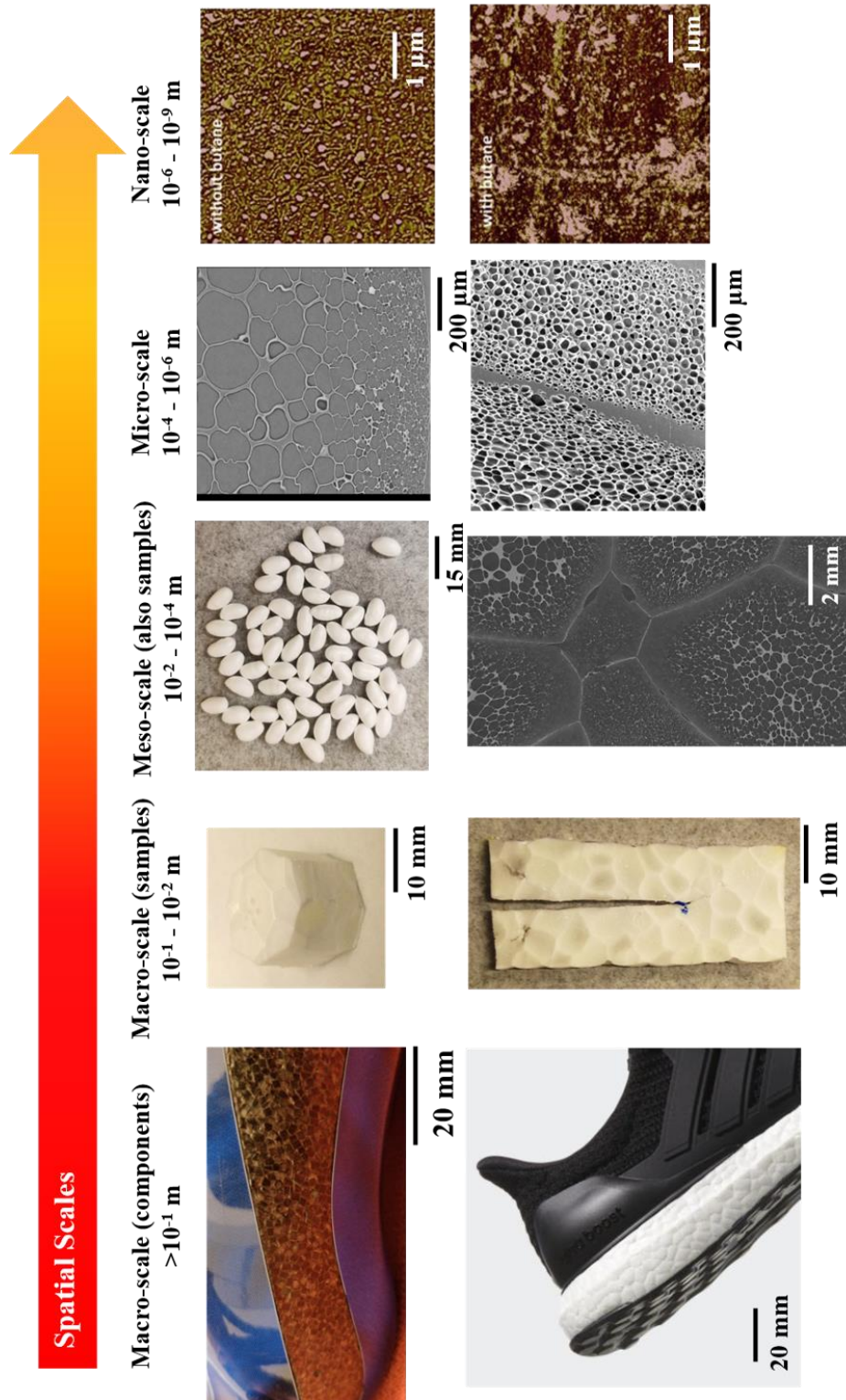


Figure 5: Structural features of bead foams (from polymer taken as an example) at different spatial scales. Illustration images at the nano-scale are adapted from Ref.[21].

Andena et al. [40] studied the compressive behaviour of expanded polypropylene (EPP) and expanded polystyrene (EPS) foam having varying densities in the quasi-static regime. Trends of increasing modulus and plateau stress with increasing density and strain rates were observed. Similar observations were reported in other studies conducted on EPP and EPS foams in compression [12, 41, 42]. This can very well be explained by the classical Gibson-Ashby model, i.e., strengthening from additional material and contribution from compression of gas within the cells represented by Equation (1).

$$\frac{E^*}{E_s} = \Phi^2 R^2 + (1 - \Phi)R + \frac{p_0}{E_s(1-R)} \quad (1)$$

where, R is the relative density, Φ is the fraction of solid contained in the cell edges, E^* is the modulus of foam, E_s is the modulus of solid polymer and p_0 refers to initial gas pressure. With increasing density, there is a direct contribution to the modulus of foam through the first term. Experimental evidence on the contribution of strain-rate hardening from the increased resistance to gas flow was shown by Bouix et al. [12]. They found the strain rate hardening rate to be strongly affected by the entrapped gas in the closed cells by conducting compression tests on EPP foams in a fluid chamber. At quasi-static loading ($\dot{\epsilon} \sim 0.01 \text{ s}^{-1}$) gas flow (indicated by bubbles in water chamber) appeared on the foam faces immediately on compression and grew slowly. With increasing strains, these bubbles became too large and left the foam when the buoyancy forces overcome the surface tension. During dynamic tests ($\dot{\epsilon} \sim 1500 \text{ s}^{-1}$), there wasn't enough time for the gas to escape until the cell was totally crushed (dense) and the internal gas was effectively trapped. This was responsible for a large increase in the cell pressure as the volume rapidly decreased, resulting in an increase in the plateau stress modulus. The strain rate effect on stress-strain curves was also seen in

shear, along with a shear hardening effect in EPP foams [14]. In contrast to compression where gas pressure hardening is substantial, polymeric contributions were attributed to shear hardening, since the tensile forces acting on stretched cell faces can result in hardening of the polymer. Here, moderating the cell face mechanical response by suitable choice of polymers (percent crystallinity, orientation of polymer chains) can alleviate the detrimental effects of shear hardening.

Voit [11, 17, 43, 44] has performed several compression studies on EPP and EPS foams at various strain rates ranging from 0.01 s^{-1} to 1500 s^{-1} . The macroscopic measurements were complemented with microscopic analysis (high speed camera, scanning electron microscope (SEM)) which revealed strong localization of the deformation in the plastic plateau region. Beads located above and below the damaged layer were intact. A multi-scale damage mechanism was observed, characterized by the local buckling of cell and bead walls. By coupling the interrupted impact methodology with microtomographic analysis the authors had more insight on the multi-scale damage mechanism [11, 44]. From a preliminary analysis of bead shapes in 2D tomographic slices, they proposed the local loading at the mesoscopic scale cannot be considered as pure uniaxial compression, rather a combination of compression and shear forces. A comparison of the density of beads (or grey level) with the observed strains from their study [11] is presented in Table 1. One can clearly tell that the densest beads are not necessarily the least deformed and vice versa, which showed that the deformation heterogeneity is not simply correlated with the density field.

Table 1 Total applied strain and local strain values of different beads in the 2D tomographic slice analysis for several impacts [11].

Bead	Surface (pixel)	Density (kg/m ³)	Strain (%)			
			Impact 1	Impact 2	Impact 3	Impact 4
1	250522	77.7	-3.7	-20	-34	-61.6
2	153920	81.3	-1.7	-8.6	-24.2	-54.5
3	245959	77.6	0	-24	-41.2	-64.3
4	274272	78.2	-4	-41.4	-59.2	-72.9
5	225409	81.2	-4	-35.2	-50.6	-67.3
Sample	4.6 x 10 ⁶	82.2	-10	-30	-50	-70

Contrary to 2D studies wherein planar displacements are assumed, from the analysis of 3D data, volumetric strain can be calculated directly from the change of bead volume and the bead displacements from its barycenter or centroid. A significant correlation between bead volume change and density (size by duality) was established, i.e., the lower the density, the greater the bead volume change [17]. Nevertheless, several 3D studies using microtomography and finite element modeling agree that the arrangement of beads, their shapes and the thickness of bead walls seem to have an influence on the strain field [17, 45]. For instance, the thicker walls could act as a more rigid secondary network altering the macroscopic response and the local deformation at the cell scale within the beads. Variability in bead density can modify the meso-scale behavior by the presence of strain localization and sometimes even alter the macroscopic response if the number density is significant.

Morton et al. [46] reported differences in collapse stress due to cell size difference in EPP foams having similar nominal density. This was also reported in the study by Bouix et al. [12] on EPP. The higher collapse stress in smaller cell size foams were attributed to a combination of factors like Young's modulus of base material, elastic buckling stress, and plastic collapse stress. Larger cell walls are more prone to bending and buckling at quasi-static strain rates, but the effect is somewhat countered by the thicker cell walls. In general, variation in cell sizes, cell wall thicknesses, curvature and corrugations (or pre-buckled ligaments) has an important influence on the mechanical response of foams [37, 47]. However, sparse are the studies on the effects of micro-scale (at the cell level within the beads) on the observed macroscopic behavior in bead foams. More important, an understanding of the bead behaviour and how this relates to the plates where the beads are bonded together, is an important question. This is an important question that will be addressed in this dissertation, which in the future can lead to a bottom-up approach to bead foam processing for an engineering application.

Another important feature in the micro-scale are the bead-to-bead interfaces formed after steam-chest molding the individual beads. The quality of interbead bonding affects the energy absorbing capacity during impact and general mechanical response since the fracture usually forms and develops in the interbead bonding regions [5, 9]. A simple method to assess the interbead bonding is to perform a tensile test and examine strengths and fracture surfaces. Ge et al. [10] compared the tensile strengths of ETPU foam made with different bead sizes under the same processing conditions and Zhai et al. [8] on EPP foams with varying steam chest parameters. Similar observations and conclusions were reported in both the studies. The tensile strength comparisons showed an increase with

decreasing bead size. Given a fixed mold dimension, smaller beads meant larger surface area, i.e., more surface of each bead could touch other beads, resulting in higher interbead bonding regions per unit volume. Fracture surfaces showed an intrabead failure (crack path ran through bead boundaries and across beads' cell structure), suggesting the strength of the beads also affected the trends. In case of larger beads, fused samples showed an interbead fracture, possibly due to lower contact area and insufficient polymer chain diffusion across the interface. However, the positive effects of foam density and interface region thickness variation can't be ruled out.

2.4. Digital Volume Correlation (DVC)

Digital image correlation (DIC) is a technique that has been widely used to measure real-time displacement and strain data by correlating the pixels in a series of images taken at different applied loads. The correlation is possible by the application of a speckle pattern on the specimen surface or the use of natural texture of the material which is tracked throughout the loading cycle to map the deformations [48, 49]. In principle, the digital volume correlation (DVC) method is an extension of the DIC technique in 3D space. By finding and tracking the same region of interest (ROI), before and after deformation, 3D distributions of local displacement and strains can be obtained [50]. Such measurements have been used to understand the fatigue crack initiation and propagation in Al-Si alloys, delamination in layered composites [51], compressive behavior of trabecular bone [49], and tensile failure in a glass filled polymer matrix composite [52]. These works use different correlation procedures and similarity measures for image registration. For instance, Gillard et al.[49] used a local approach to DVC, wherein the ROI is divided into

small non overlapping sub-volumes. The registration was performed independently on each sub-volume without dependency on the neighboring sub-volumes. Conversely in the global approach, the registration is performed over the whole ROI [51]. Roux et al. [18] developed a new correlation algorithm to study the meso-scale and micro-scale deformation in a PP bead foam. They were able to show the strain localization at the cell level within a single bead, with a cubic ROI of 176 voxels. It is not clear if this algorithm can be applied to large datasets without a huge computation penalty. Foam datasets usually lack or have small grayscale variation in the whole image suggesting that correlation methods might present its own challenges in image registration for DVC. In addition to the correlation methods, the image registration and bulk displacements in DVC can be done by tracking features (micro-pores, cracks, second phase particles). In the volume of work available on DVC using particle tracking, systems have been carefully chosen, i.e., features naturally with high contrast from matrix (quick image segmentation) or artificially introducing markers [48, 51, 53]. Though the contrast in the system of interest is uniform between voids and ligaments (see Figure 25 (d)), the segmented voids in the foam were used as markers in an individual bead foam (Chapter 3) and molded bead foams (Chapter 4). A complete 3D strain field thus can be obtained which can help in understanding the correlation between material texture and deformation [18].

2.5 Research Objectives

In this research, we have focused on individual eTPU bead foams as well as bonded layers used in the midsole of high-performance footwear. The intention is to obtain a thorough

understanding of the deformation behaviour at the meso and microscale, in individual beads and bonded plates, when subjected to compressive stresses.

The objectives of the current research are:

1. Study the evolution of damage and its dependence on the microstructure by performing *in situ* experiments using x-ray microtomography.
2. Perform DVC on 4D datasets for quantitative volumetric deformation and to map local strains.

CHAPTER 3

IN SITU X-RAY MICROTOMOGRAPHY OF THE COMPRESSION BEHAVIOR OF ETPU BEAD FOAMS WITH A UNIQUE GRADED STRUCTURE

3.1. Introduction

Foams are ubiquitous in our modern world, ranging from novel sandwich foam cores in aerospace to simple packaging materials [54–56]. In recent times, bead foams have received a lot of attention due to their ease in filling intricate shapes compared to conventional foams. Several papers have focused on understanding the morphological development, processing techniques, and on techniques for developing polymers suitable for bead foaming [1]. In particular, thermoplastic polyurethane [2] has been used to make beads that are used extensively as the midsole of adidas ‘Energy BOOST’ running shoes. The function of the midsole is to absorb the energy generated as the foot lands while keeping the peak force below a certain threshold, minimizing the chances of injury [57]. These characteristics come from the peculiar stress-strain behaviour displayed by these materials which can be altered by changing the deformability of the cellular structure.

The mechanical properties of bead foams used in midsoles depends strongly on the cell geometry, ligament thickness, gas properties and the constituent material per work done on closed cell foams [14, 37]. Bead foams are routinely moulded into a plate. The effect of density and strain rate on the global response of bead foams in moulded form has been investigated [11–14]. Much like closed cell foams, the moulded beam foam stress-strain behaviour exhibits three regimes: an elastic behaviour followed by a stress plateau, and at higher strains, a rising hardening regime due to foam densification.

Over the last two decades, the use of micro X-ray microcomputed tomography (XCT) has become an essential technique for non-destructively characterizing the distribution of second phases, damage evolution, corrosion behaviour, and other aspects of mechanical behavior [58–62]. *In situ* examination of polymeric foams has been conducted using both laboratory and synchrotron x-rays [63–65]. Unlike traditional destructive techniques, XCT enables a time-resolved understanding of physical mechanisms under various conditions in three dimensions (3D) and is well suited for stochastic structures, such as bead foams. This is possible using complementary techniques that are combined during the analysis. The microstructures obtained from XCT can also be exported to finite element models to model the deformation behavior [55, 60, 66, 67]. A complementary approach is to determine the internal volumetric deformation and correlate the heterogeneous structure with local displacements (and strains) by digital volume correlation (DVC) [18, 48, 52].

A thorough understanding of mechanical behaviour of individual bead foams is lacking. Furthermore, the influence of local pore distribution and gradation in pore size, with the stress-strain behaviour of the bead, needs to be understood and quantified. In this work, we have studied the deformation behaviour of an expanded thermoplastic polyurethane (eTPU) bead foam, used in the midsole of footwear, under compression. Lab scale micro-CT was used to image its internal cellular structure in an interrupted *in situ* fashion at small strain increments. 3D image analysis was performed to investigate the local microstructure and was correlated to the stress-strain behavior. The strain evolution was quantified using digital volume correlation (DVC) principle. Mechanisms of void collapse buckling, the rate of changes in void volume, and the influence of structural

heterogeneities on mechanical response were explored experimentally and analytically and are discussed.

3.2 Material and Methods

3.2.1 General overview of testing

The eTPU bead foams used in this study were Infinergy® 32-100 U10 beads manufactured by BASF with a resulting bulk density of 85-135 kg/m³. Three bead foams were selected at random for investigating their initial microstructure, as well as changes with externally applied compressive strain, using a lab-source x-ray microtomography system (Zeiss Xradia Versa 520, Carl Zeiss XRM, Pleasanton, CA, USA). Please refer to Table 2 for scan details of the samples. A compression loading stage was especially designed to be compatible with the lab-scale CT system [68]. The experimental setup is shown in Figure 6. The loading stage consists of a mechanical setup capable of translating the top platen downwards, when the screw (see Fig.6.b) is pushed into the platen. A known displacement was imposed (to achieve a desired strain) by calculating the number of turns and pitch of the screw. The bottom platen is fixed and has provision for integration of a load cell (see Fig.6.b). The platens are made of low friction PTFE to avoid frictional effects at the contact zone during compression. An x-ray transparent sleeve using PMMA houses the setup and was compression fit into the fixture to directly go on to the rotation stage.

Table 2 Details of the x-ray scans of different samples along with their strain state during imaging. LR and HR denotes low-resolution and high-resolution scan respectively.

Sample	Strain state (%)	Scan Type	Voxel size (μm)	Scan Time (h)
A	0 and 50	LR, HR at the free side	LR-4.2, HR-1.3	LR-8.3, HR-11.1
B	0 and 50	LR, HR near the bottom platen	LR-3.1, HR-0.9	LR-11.1, HR-11.1
C	0,5, 10,...,50	LR, HR near bottom platen	LR-3.7, HR-0.9	LR-11.1, HR-16.7

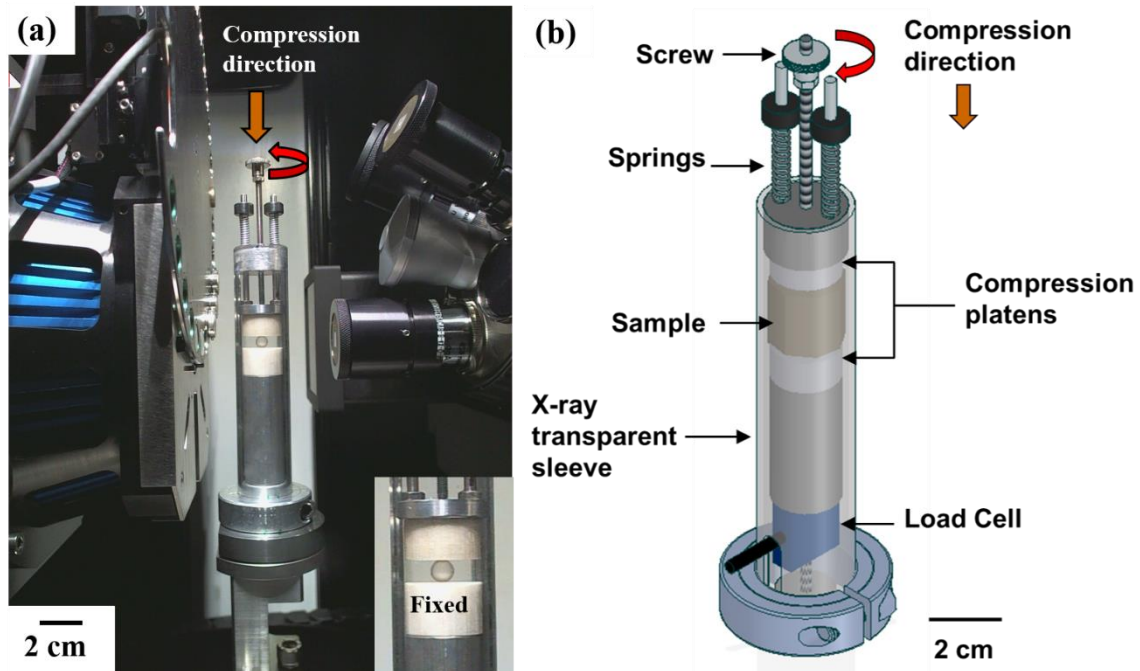


Figure 6: (a) Experimental setup of compression in the lab scale CT system with the loading fixture. Inset shows the top and bottom platens at a higher magnification. (b) Schematic of the loading fixture.

3.2.2 Interrupted *in situ* CT

An individual bead foam was loaded between the platens in the loading fixture and a full CT scan of the sample at a lower resolution (LR) was taken at zero strain. Subsequently, a higher resolution CT scan of a small region of the sample near the bottom platen was taken, since these bead foams have microstructural heterogeneity within cell structure, as shown by the cryo-sectioned SEM cross sections shown in Figure 7. The use of terms lower and higher resolution is to emphasize the difference in voxel size used (refer Table 2) and does not suggest a limitation of the technique. The bead was compressed in increments of 5% strain, by the clockwise-rotation of the screw (see Figure 6 red curved arrow), which imparts a downward motion of the top platen (see Figure 6 orange arrow). A combination of HR and LR scans, as mentioned above, was taken at every externally applied compressive strain. Care was taken to allow for enough time to elapse after compressing to the appropriate strain, so that stress relaxation would not lead to image blurring during the CT scan [63].

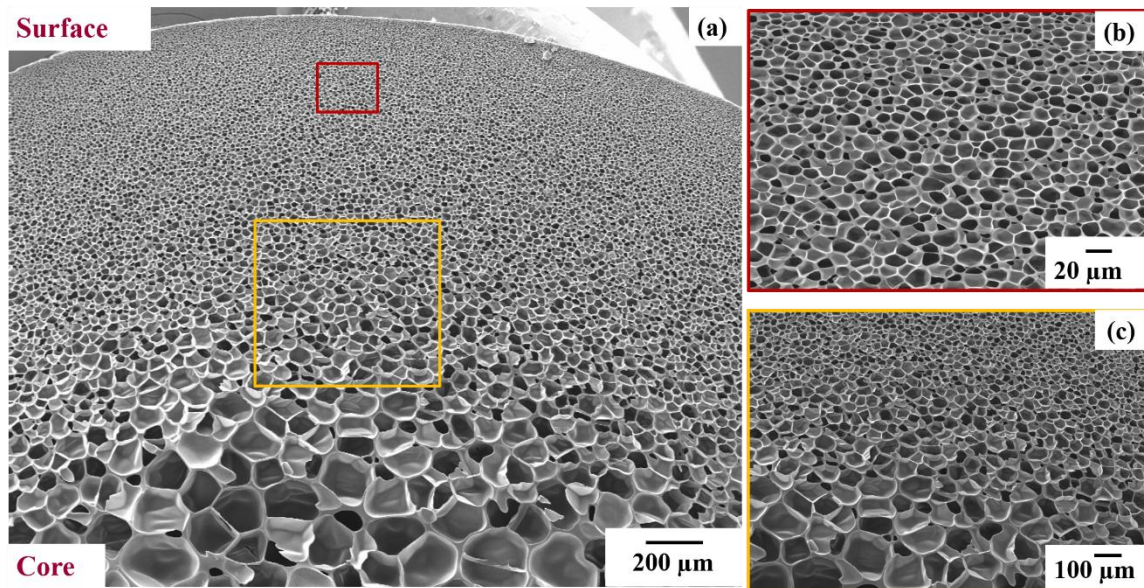


Figure 7: SEM image of the cryo-sectioned bead foam surface showing the variation in void size and ligament thicknesses from the surface to core of the bead. (a) Low magnification view showing half the bead. (b) and (c) High magnification images of the regions within the red (close to surface) and orange (transition area) boxes in (a).

3.2.3 Image analysis

Sinogram images were used to obtain a 3D reconstruction using a commercial software package (Zeiss XMReconstructor), which uses an algorithm based on a standard filtered back-projection algorithm. For data processing, the reconstructed 3D tomograms were processed using Avizo (Version 9.0.1, FEI Visualization Sciences Group, Oregon, US) and MATLAB R2018b. The raw images were filtered using a diffusion-based smoothing filter (non-local means) followed by a sharpening filter (unsharp mask) to reduce noise, reinforce the contrast at the edges, and make details appear sharper in the dataset. Image analysis was then carried out on the 3D data sets for quantitative analysis by two routes. A simple grayscale threshold was used to obtain the binarized image, which was eroded and dilated to fill isolated islands of pixels inside the void. Flowchart of this routine is shown in Figure 8. Thereafter, void equivalent diameter and ligament thicknesses were computed on the zero strain datasets. Conventional methods fail to consistently binarize the data in the same manner due to complex buckling, as well as variation in grayscale values resulting from density changes during compression. Thus, the region growing technique [69] was used on datasets planned for DVC, which selects the largest connected area in 3D that contains the manually placed seed voxel and all voxels with grey values lying inside a user defined range. The DVC datasets required identifying and labelling of the voids using the same

“IDs” to ensure a one-to-one correspondence when tracking local displacement and strains, as a function of applied strain. Only a limited number of voids were identified in the HR and LR datasets for the purpose of strain mapping through DVC.

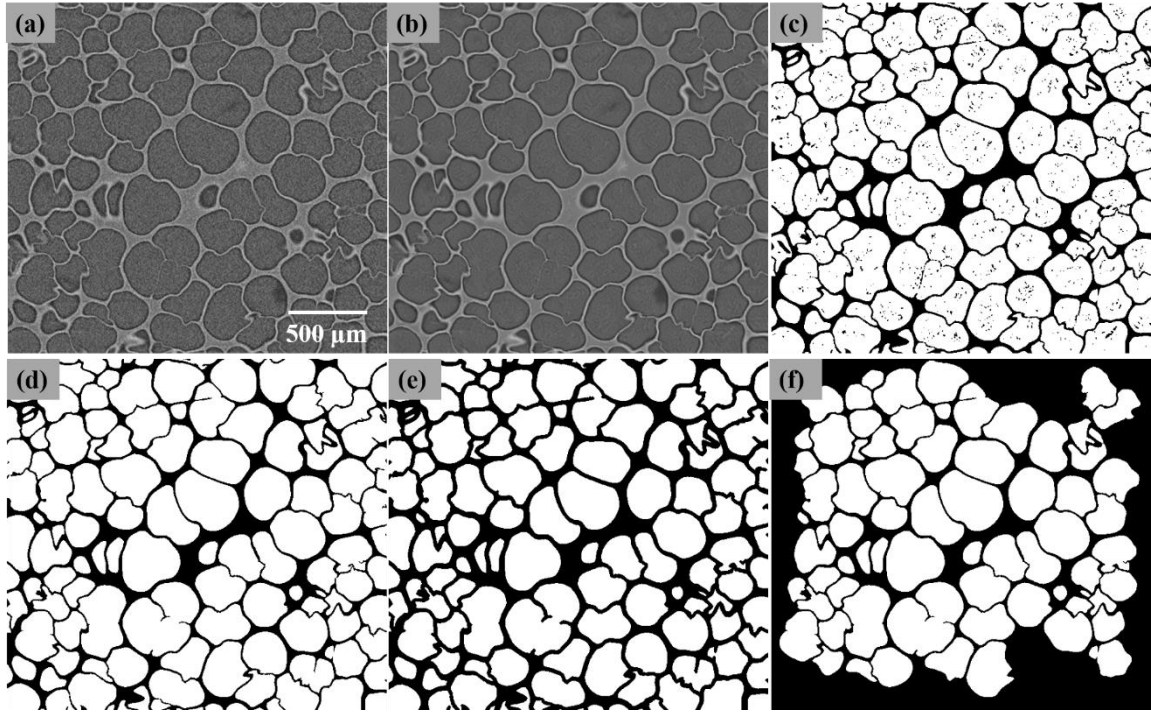


Figure 8: Image analysis workflow with the different steps during the process. (a) Grayscale image, (b) Filtered image, (c) Thresholded image, (d) Dilated image, (e) Eroded image and (f) Border killed image.

3.3 Results and discussion

3.3.1 Morphological characteristics

A virtual CT slice of the experimental sample from the mid-section, before compression, is shown in Figure 9. A 3D rendering of a portion of the sample is shown in Figure 10 (a). A region near the surface of the bead is shown in Figure 9 (b). The bead morphology shows

fewer and larger cells near the bead center and a higher cell density region near the bead skin. This is characteristic of the vessel expansion batch-foamed beads [3]. Herein, the solid beads impregnated with blowing agent are released from the vessel and foaming occurs due to the sudden drop in pressure. Cells start to nucleate and grow within the polymer matrix creating the foamed beads. During this process, blowing agent could escape to the environment before cell stabilization leading to low gas concentration near the skin. Consequently, we are left with a structure of smaller cells in the skin and larger cells in the center. The structure of this closed cell bead foam is complex, as shown in both Figure 7 and Figure 9, consisting of a range of cell sizes, solid cell walls with varying thicknesses, curvature, and corrugations (or pre-buckled ligaments). Each of the above has an important influence on the mechanical response [70] and computing these can help us identify clustering of locally weak and strong zones in the microstructure. However, only void sizes and ligament thicknesses were quantified in this work, and the other features were used for qualitative comparisons during the analysis of deformation.

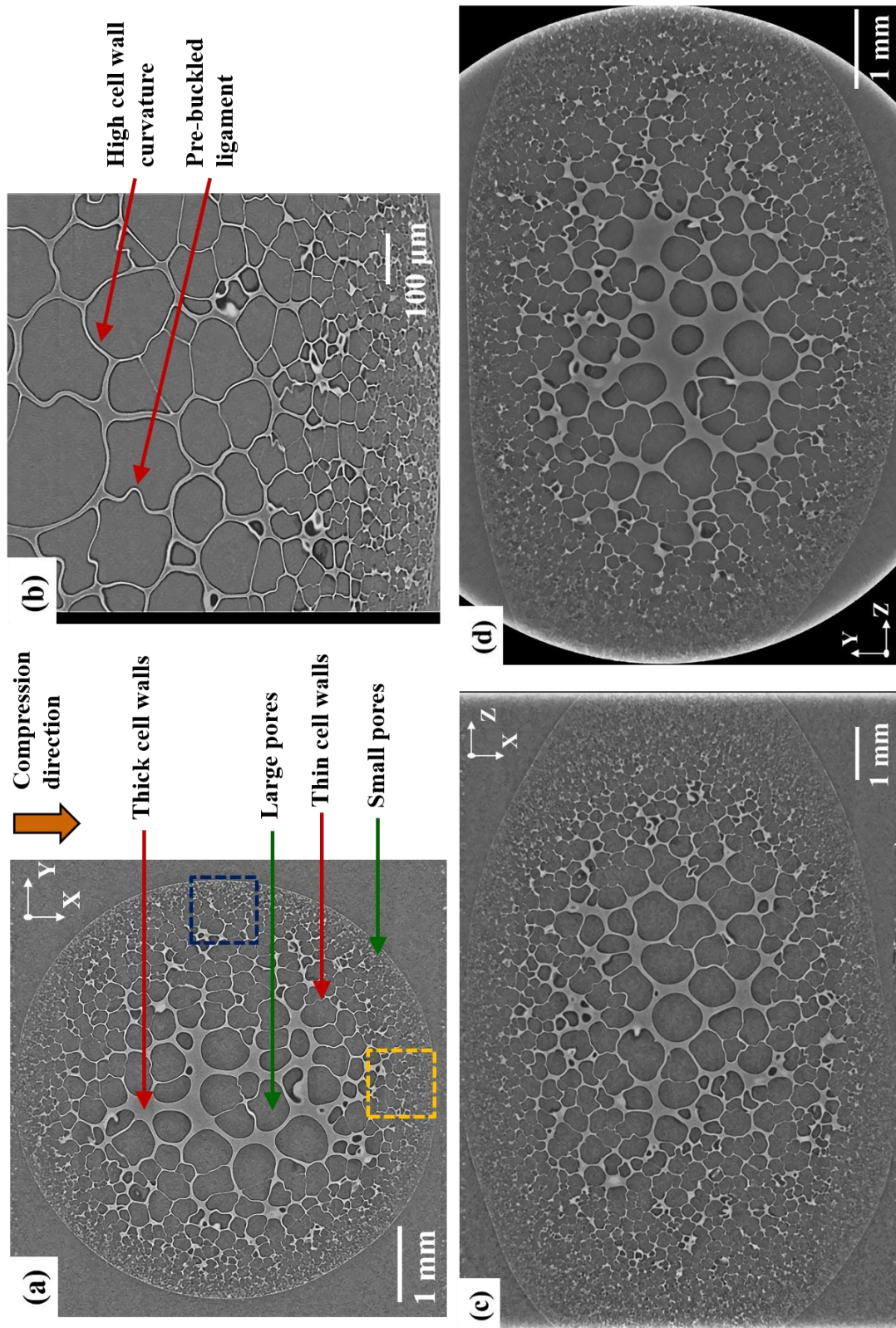


Figure 9: X-ray CT slice from the mid-section of sample before compression at zero strain showing the heterogeneity in cell structure. (a) Slice from LR scan of whole bead along compression direction. (b) Slice from HR scan of the region within the dashed orange box (close to the bottom of the image) in (a). (c) and (d) Slice in the XZ and YZ axis, which are orthogonal to (a). The compression axis is along the X axis.

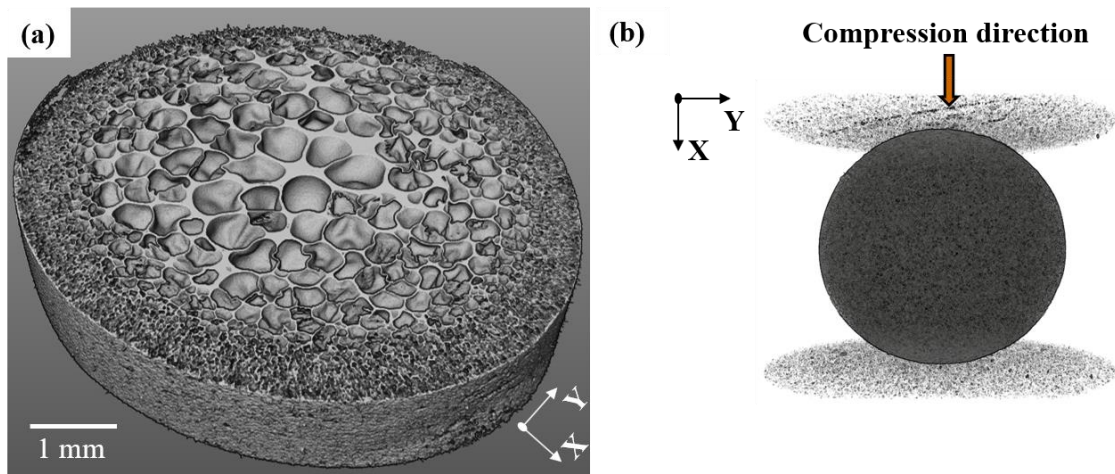


Figure 10: (a) 3D rendering of the foamed bead, (b) 3D rendering of the compression of foamed bead with the coordinate system used throughout this chapter.

Figure 11 shows the void size distribution of all the three samples before compression. Void size here is represented in 1D by reporting the diameter of an equivalent sphere of the same volume. The segmented voids were chosen randomly along various position in the beads for quantification, since the entire volume was too large to be thresholded. The spatial variation in void sizes in these bead foams ranged from 20 μm to 700 μm and is nearly symmetrical along the compression direction. A perfectly symmetrical hypothetical distribution is also shown as reference in Fig.11 (e) and (f). This near symmetry seen in the compression axis (X) was also observed in the other orthogonal axis (along Y) to compression as understood from Fig.11 (d)-(f) and indicates an overall

radial variation in cell size. Similar trends in all the three samples examined, demonstrates the control and reproducibility of the foaming process. Such a systematic variation of void sizes from the surface to core is typical in functionally graded porous materials (FGMs) and possess advantageous physical and mechanical properties [56, 71, 72]. In the next section, we explain the role of this morphological variation in the response seen during compression.

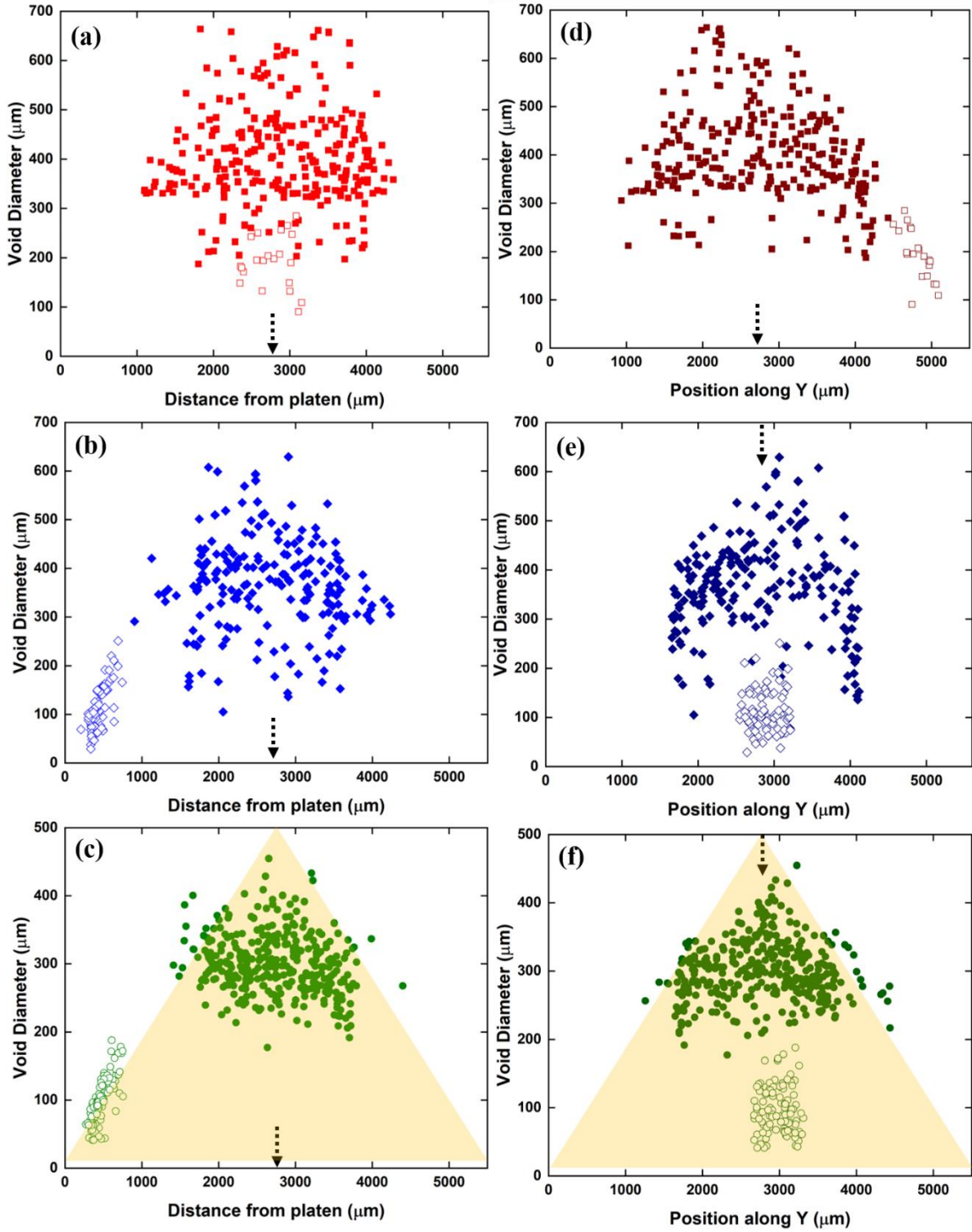


Figure 11: Plot of void position against its diameter showing the variation in size from surface to core of the sample along the compression axis (X) and orthogonal to it (Y). a, b

and c are data along compression of Sample A, B and C. d, e and f are data along orthogonal direction to compression of Sample A, B and C. Open symbols represent data from HR scans, while filled symbols represent data from LR scans. Dashed arrow indicates the centre of the sample along compression axis. Hypothetical distribution is shown as the region bound within the triangle in c and f.

3.3.2 Structural changes during compression

Figure 12 shows the rendering of the sample under compression at 0 and 50% strain. Since there is no constraint on the sides, there is lateral deformation in the bead. By visual examination of the sample in the compressed state, we observed that the external shape change is uniform across both halves of the bead. This proportionality is believed to be a result of the spatial variation in the morphological features and will be discussed in detail.

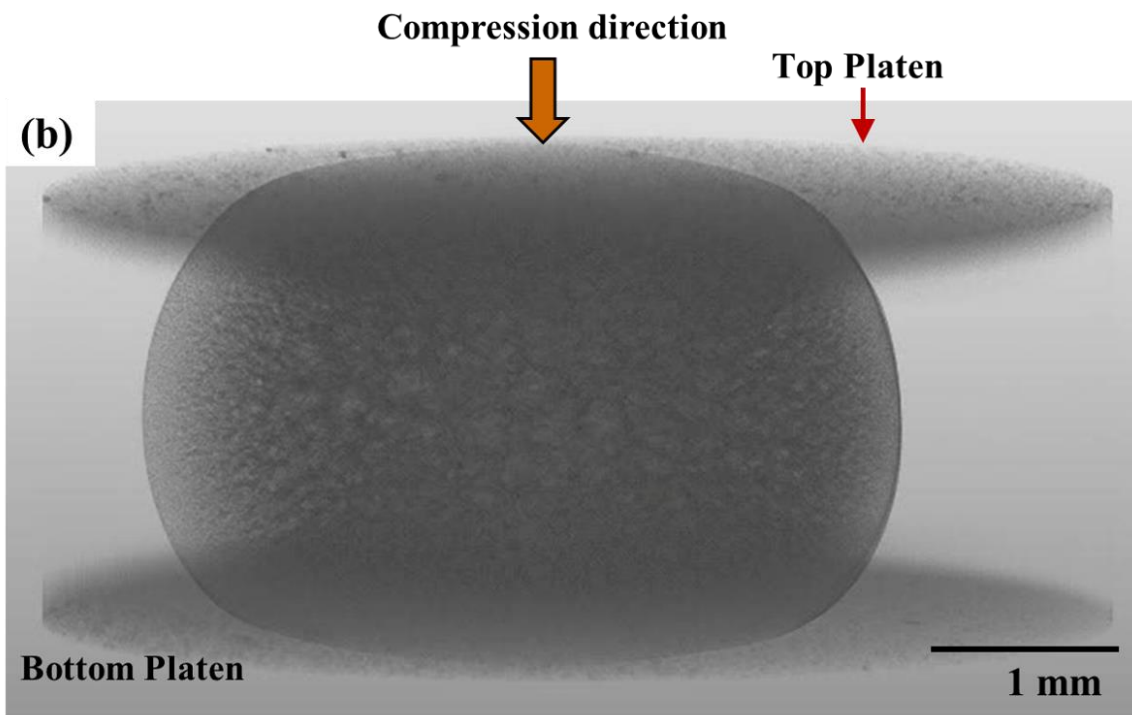
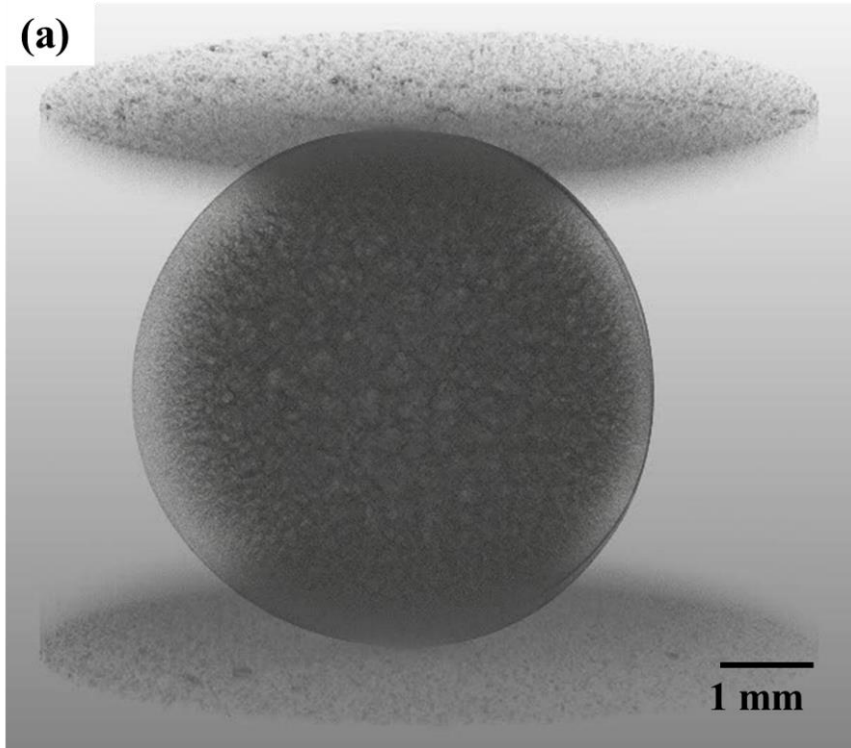


Figure 12: Grayscale volume rendering of the bead taken at (a) 0% strain and (b) 50% strain showing the external shape change. The platens are shown as a thin disc for clarity.

Deformation of sample C mid-section during compression is shown in Figure 13 in incremental steps of 10% applied strain between 0 and 50%. The section doesn't necessarily display the same voids throughout due to material from another plane coming into this plane and vice-versa. A feature in the bottom platen was used as reference for selecting the sections. By comparing the images, we notice that the deformation occurs at the contact surfaces and spreads inwards (from the platens towards the central region) as the compressive strain increases, which is analogous to the contact of a rigid flat surface with an elastic sphere described effectively by the Hertzian contact theory [73]. Interestingly, the contact surfaces on the upper and lower contact boundaries are very similar in size throughout the entirety of deformation. This is indicative of a similar local stiffness of the bead at its top and bottom portions and is highly dependent on the internal cellular structure of the bead. We attribute this behavior to the near symmetrical distribution of voids and increase in ligament thickness from the surface to core. In fact, similar observations of local stiffness were reported in a functionally graded porous beam with a symmetric porosity distribution [74].

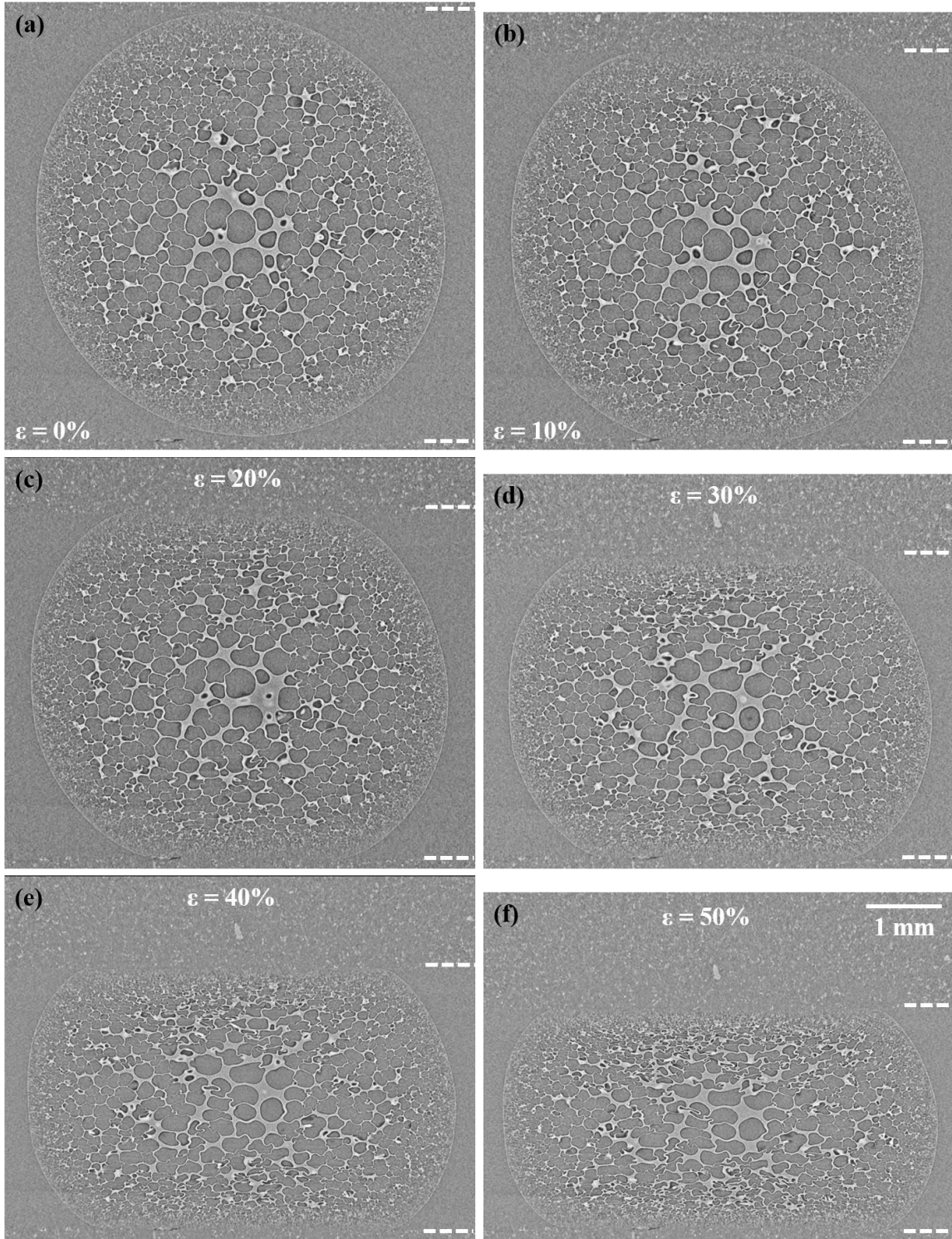


Figure 13: (a-f) Grayscale image of mid-section of Sample C under compression in multiples of 10% strain increments from 0 to 50% strain. The top and bottom platens are marked on one end for clarity.

Consider the case of a symmetric cell size distribution mentioned in Chen et al. [74] which only has an increasing cell size from the outer region towards the center. Such a distribution under compression would show severe strain localization and lead to global instability. This is due to the low-density central region having large voids, and weaker compared to the high-density outer region. However, in our case, an increase in ligament thickness in tandem with the rise in void size is seen from the skin to the center. This meant that the density should nearly remain the same, and there were no bands of minimum stiffness to being with. This is manifested by the absence any deformation bands in Figure 13. To confirm this absence, we visualized the change in volume of randomly segmented voids at different locations in the sample at multiple strains, as shown in Figure 14. As expected, the voids near the platens are more compressed than the ones in the central region of the bead. At higher strains, the decrease in void volume has a plane of symmetry in the center. This is indicative of the stability of the structure resulting from the radial variation in ligament thickness along with cell size. The other advantage of having relatively thicker ligaments in the core is seen by the small change in void volume as we move to the center of the bead, even at strains as high as 25%. These thicker ligaments act as anchoring points and only buckle at larger strains. Such moderation of the post-buckling behavior of these foams from the increase in ligament thickness from surface to core can improve energy absorption [71, 72].

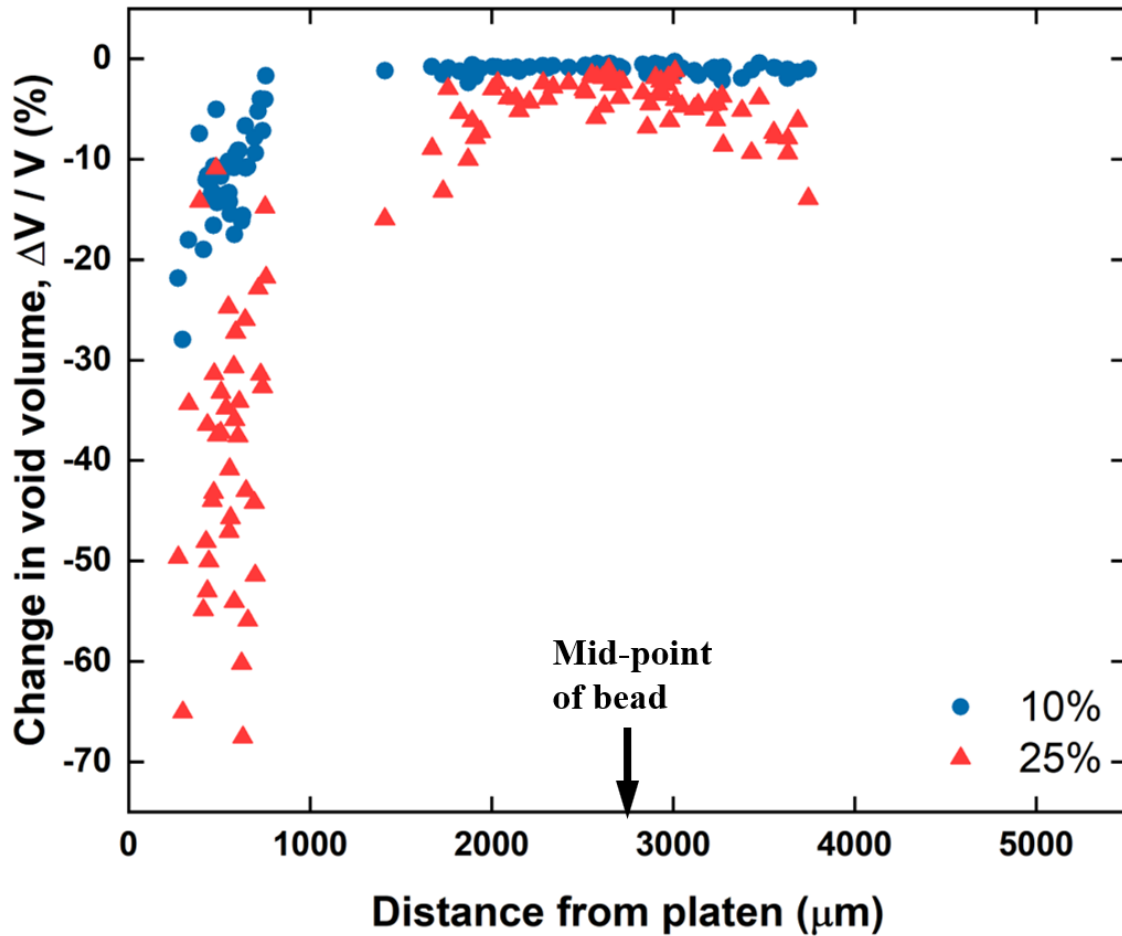


Figure 14: Plot showing the change in volume of voids in Sample C at different position along the compression axis at 10% and 25% applied strain. The centre along this axis is marked by a dashed arrow.

From Figure 13, it is also evident that increasing engineering strain also increases the lateral deformation homogeneously. It is possible that this is due to the lack of constraint at the sides, leading to indirect tensile forces acting on some portion of the bead. With the progress of deformation in the bead foam, the transmission efficiency of applied strain to the central core decreases due to the strengthening from thicker ligaments at the core. In addition, since we have a radial variation in structural features, there is an internal structural

symmetry, but out-of-plane to compression axis (Y, see Figure 9 (a), Figure 10 (a) and Figure 11 (f)). The buckling of the cellular structure at this mixed strain state seems to be steady which is revealed in Figure 15, which shows a 2D section near the free bead boundary at 0 and 50% strain. Such a graded structure with increasing void size and ligament thicknesses, with near symmetry in 3D is quite original and stems from the unique processing.

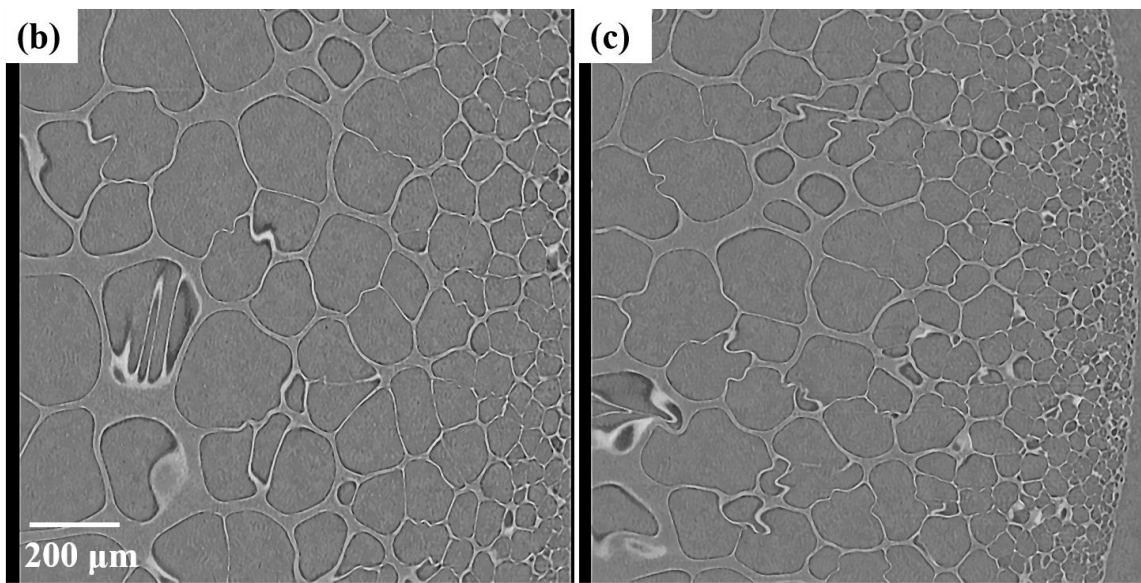


Figure 15: Grayscale image close to the free surface of the bead under compression at (a) 0% and (b) 50% strain. ROI shown is marked with dashed blue line in Fig.9.a. Compression axis is in the plane of the figure, top-down.

Figure 16 shows the grayscale 2D slice from the HR scans of sample C near the bottom platen during compression. Consistent with observations from previous work on metallic foams [60, 61], deformation occurred in the weak cell wall region. The load is then subsequently transmitted to nearby cell-walls and junctions. The material resists against bending and buckling, until the next weakest region of cell-walls will begin to

collapse, leading to densification. The fact that the deformation advances through local instabilities suggests that the cell structure and its relation to those of neighbouring cells plays a significant role [61]. However, in our case, the contact surface of the bead is changing continuously due to point contact loading of bead between the rigid platens. Hence, the initial position of the void might also influence the neighbourhood problem.

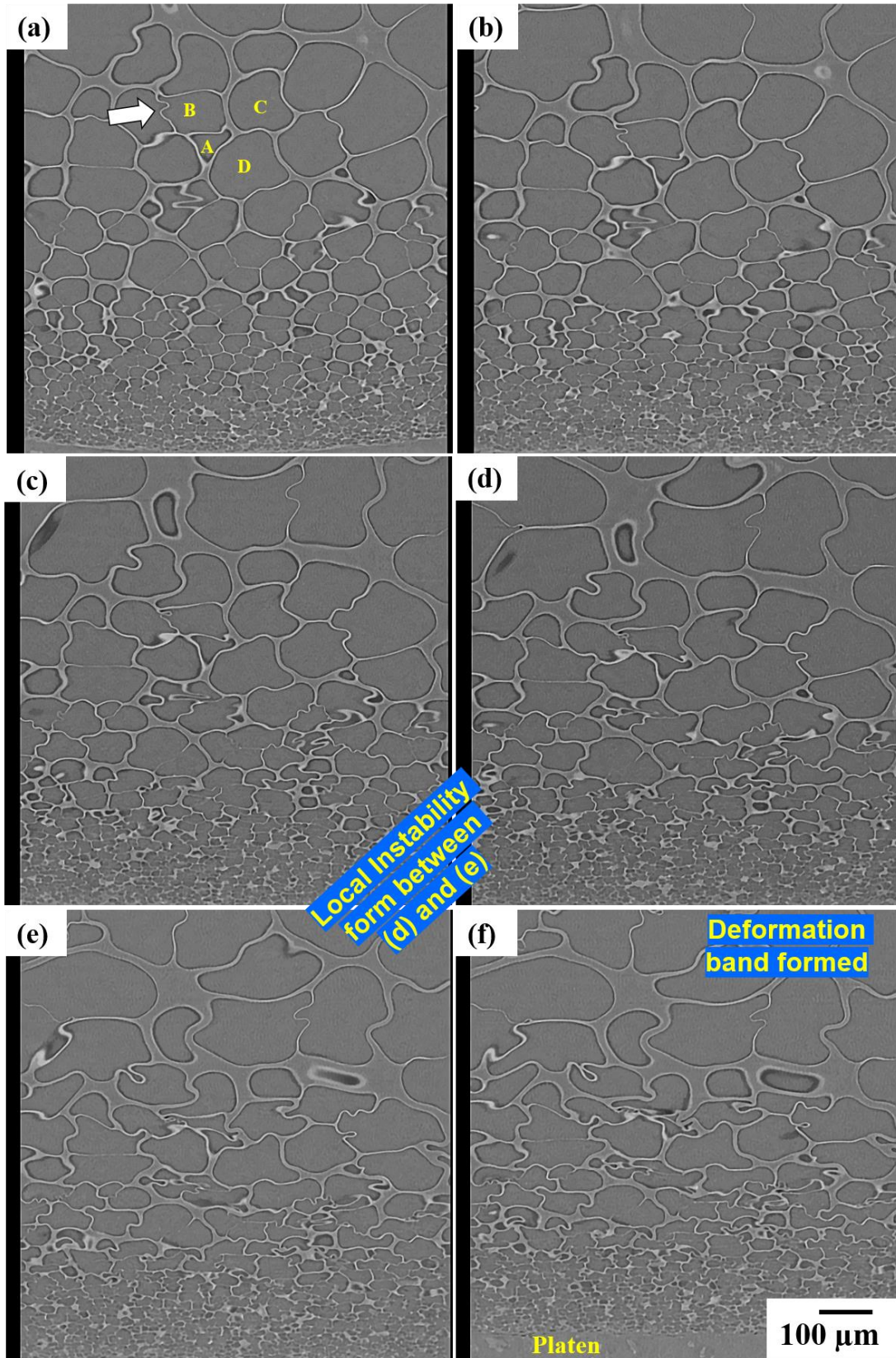


Figure 16: (a-f) Grayscale image of same section from the HR scan of sample C near bottom platen in increments of 5% applied strain from 0 to 25%. Bottom platen is noticeable only in (a) and (f). Compression direction is in-plane to the figure (top-down). White arrow points to pre-buckled ligament. Red and Yellow arrow points to cell-walls of void C having different initial curvature.

3.3.3 Local deformation inhomogeneities with aid of strain maps

In the previous section, we have shown that the global stability of the cellular structure is a result of the near symmetrical distribution of void size and ligament thicknesses. Here we attempt to look at the local stability of the voids by combining the use of segmented voids and the strain maps obtained from DVC. A brief introduction to the analysis scheme used in this work is introduced before using the strain maps.

From the *in situ* CT datasets taken under compression, we obtained a 4D dataset, i.e., 3D data sets as a function of time. MATLAB codes were developed and used to volumetrically map the strain evolution inside the sample during compression testing. A general overview of the DVC method has been described elsewhere [51]. In our case, we used a reference state and a deformed state to calculate a three-dimensional displacement field based on tracking the voids. A schematic of this method along with the algorithm is described later in Section 3.3.3.1 and shown in Figure 18. Only the voids segmented using the region growing technique were used as markers. Then, the displacement field is converted to a strain field for the three primary volume directions (ϵ_{xx} , ϵ_{yy} , ϵ_{zz}). The loading direction, which was parallel to the compression axis, defined here as being parallel to ϵ_{xx} . Strain maps were computed for both the HR and LR datasets of sample C only.

3.3.3.1 Local Strain Distribution by DVC

Figure 17.a shows the rendering of voids segmented near the bottom platen with a semi-transparent overlay of foam structure. Figure 18 shows a schematic of the DVC routine applied ((a)-(d)). As mentioned earlier, we tracked the voids for the correlation between two consecutive applied strains (see Figure 18 (a) and (b)). This is analogous to tracking microstructural features in the work by Kobayashi et al. [53]. Since the voids are compressible, their centroids were used as landmarks for this correspondence problem. It will be shown later that the strain maps resulting from the use of these landmarks are fully capable of identifying mechanisms of local pore collapse. At first, the displacements are obtained for the tracked voids by subtracting their centroids in 3D space.

$$Displacement_i(d_{i,x,y,z}) = p_{i,x,y,z} - q_{i,x,y,z} \quad (2)$$

In this manner, we have sparse displacement data only at the location of centroids (see Figure 18 (c)). To avoid a computationally intensive process, the correlation and calculation of displacement field was limited to volume bounds, surrounding the void centroids. The volume bound is a convex hull passing through each marker which is shown as a still image in Figure 17 (b) and in 2D in Figure 18 (d). A natural neighbour interpolation scheme in MATLAB [75] was used in establishing the relationship of every non-landmark voxel within the volume bound using those of the landmarks using the in-built function *scatteredInterpolant*.

$$F_k = scatteredInterpolant(p_{i_x}, p_{i_y}, p_{i_z}, d_{i_k}, natural) \text{ for } k = x, y, z \quad (3)$$

Strains were obtained by taking partial derivatives (in-built function - *gradient*) of the displacement field, which gives a measure of how rapidly the displacement changes in a deforming material.

$$e_{kk} = \text{gradient}(F_k) \text{ for } k = x, y, z \quad (4)$$

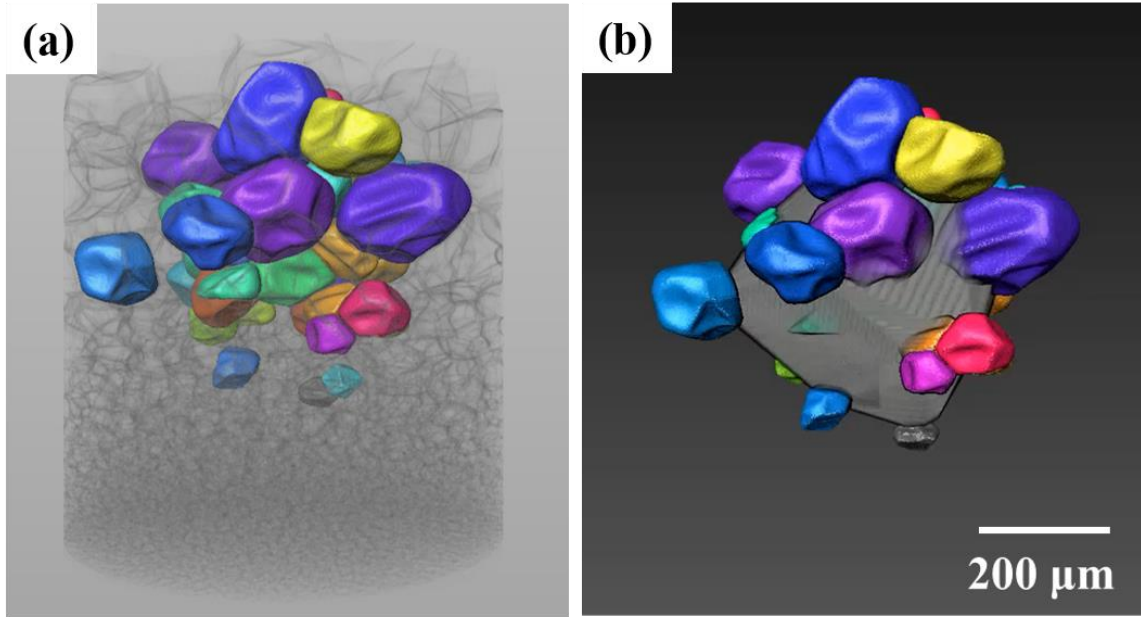


Figure 17: (a) Visualization of the voids used as markers in DVC and (b) Volume bounds encompassing the voids for calculation of displacement field. Void colouring is random and is unconnected. Void renderings are from the HR scan of sample C at zero strain. Foam structure is shown semi-transparent in (a).

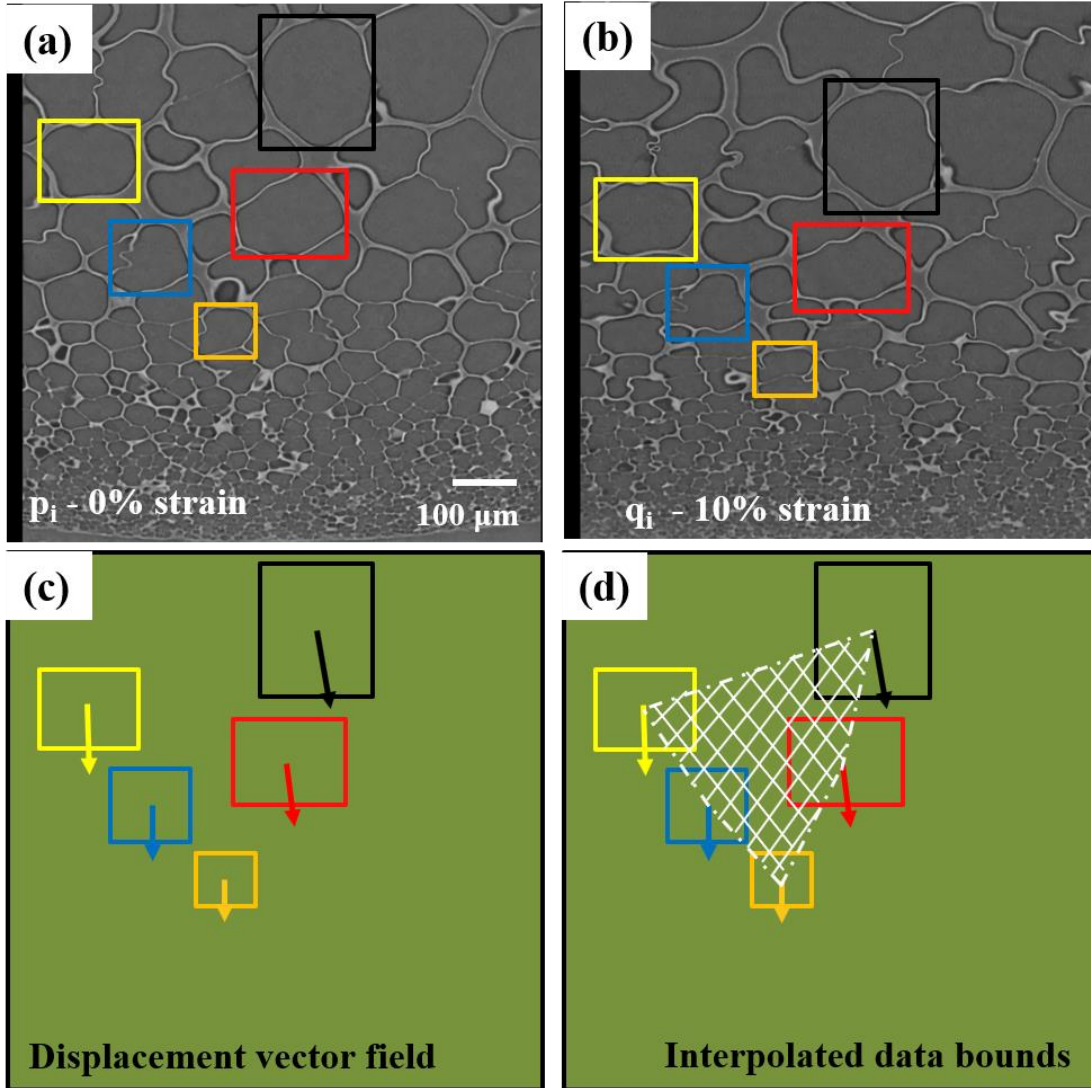


Figure 18: (a) - (d) Schematic of DVC routine with help of 2D visualization.

Figure 19 (a) shows the strain distribution in the central region superimposed on its grayscale image at 5% applied strain. Strain distribution in the region of the sample marked in Figure 19 (a) near the bottom platen is shown in Figure 19 (b). Displayed strains are along the compression direction, i.e., ϵ_{xx} . The irregular boundary where there is a uniform color corresponds to the area of near zero strain. It corresponds to the section beyond volume bounds at this planar cut. The volume bounds represent the 3D region within which correlation and interpolation was computed using a convex hull wrapped around the

markers. On slicing through the dataset, the bounds show up as an irregular polyhedron. The strain values in Figure 19 (b) gradually drop as we move away from the platen and is consistent with the previous comment on the deformation contact zone. Note the range of the color bar and the uniform nature of strains in Figure 19 (a), indicative of the same. A comparison was then drawn with the externally applied strain and the engineering compressive strain totalled through DVC from different regions in the sample, as shown in Figure 19 (c). These are local mean values, i.e., calculations were limited to a small sub-volume within the bead. The steep increase in strain near the bottom platen, and the gradual increase in strain in the central region demonstrates the likely variation in cell deformation due to the gradual progression of load from the contact surface into the core of the bead. This trend seen in Figure 19 (c) obtained from the small sub-volume of the tomogram agrees with the observations made from both Figure 13 and Figure 14. The measured strain at 50% compression near the free surface at the sides was low, since this zone was outside the direct influence of applied strain. Strains from DVC using the voids as markers are clearly able to capture the global behavior seen in these foams.

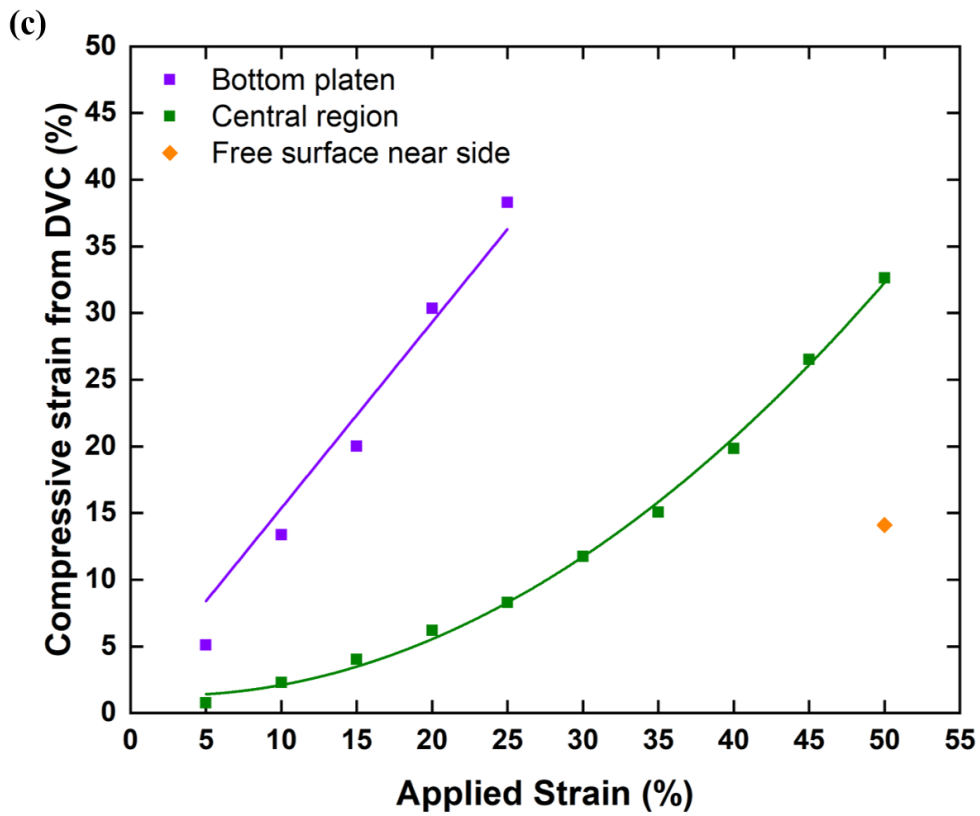
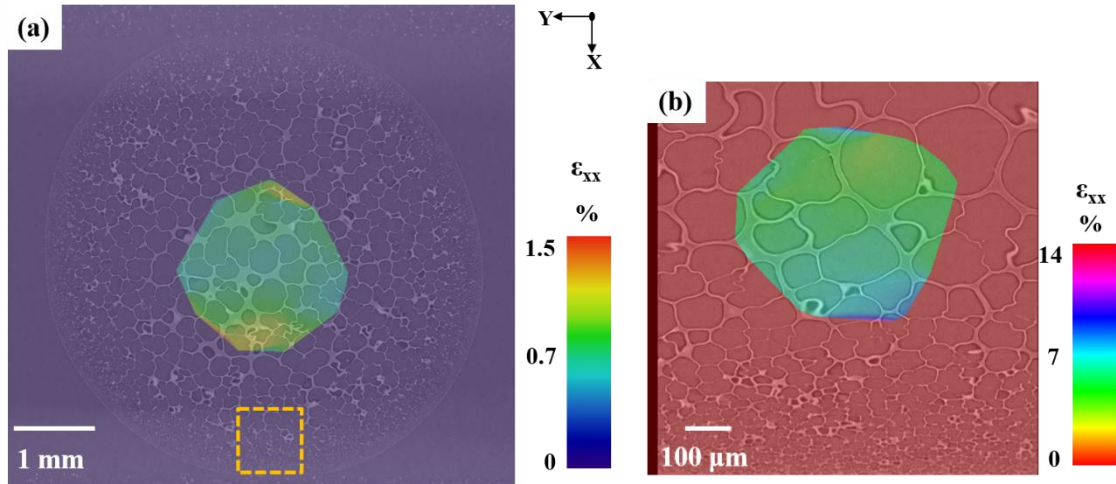


Figure 19: (a) Strain along loading direction (ϵ_{xx}) in a bead foam under compression computed from DVC. (b) Strain field of region near platen marked in (a). (c) Plot showing the correlation between the externally applied strain against the measured strain along the compression direction using DVC in different regions.

3.3.3.2 Local void collapse and deformation instabilities

To understand this better, we tracked a group of four adjacent voids labelled A-D in Figure 16 (a) and its deformation with respect to the original size and shape is presented in Figure 20 (a) and (b). The selected void A is relatively large compared to the others considered here and is without any extreme irregularity in shape. The complex wrinkling observed in voids B to D suggest the presence of either a large cell-wall curvature or a pre-buckled ligament in the as-processed state (see Figure 20 (b), $\epsilon=0$). From Figure 20 (a) we notice that the voids further away from the contact surface (B and C) have deformed by a large amount, at an applied strain of 25% compared to voids A and D. In the case of void B, from the its shape change (see Figure 20 (b)), there is strain localization around the weak regions, but the situation pertaining to void C is quite different. Up until $\epsilon=0.15$, the deformation in void C was dominated by the effect of its position, in comparison to void A and D. This can be explained by the point contact of bead with the platen. The deformation zone progresses from the region near the platen toward the central core. Clearly, positional effects outweigh the variation in microstructural features, at least until full contact with the platen is obtained. However, at $\epsilon=0.20$ severe heterogeneity in the trends of void volume changes are noticed. Both these variabilities are clarified with the help of strain maps shown in Figure 21. For the sake of brevity, ϵ_{xx} and ϵ_{yy} data at 5 and 15% strain are shown.

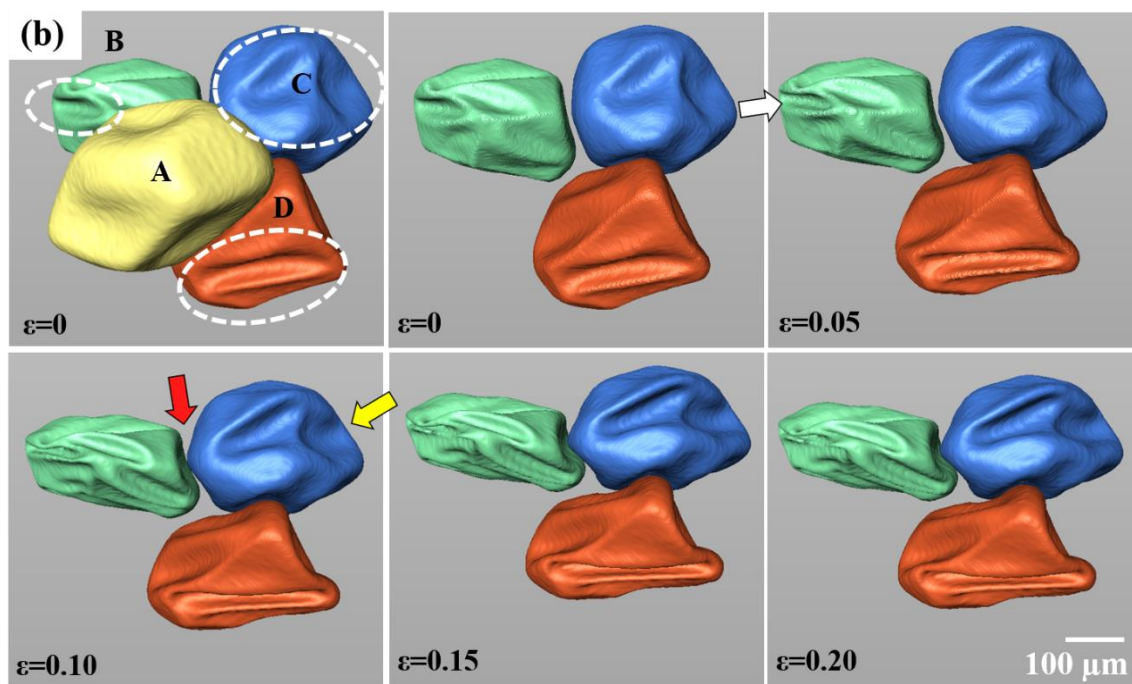
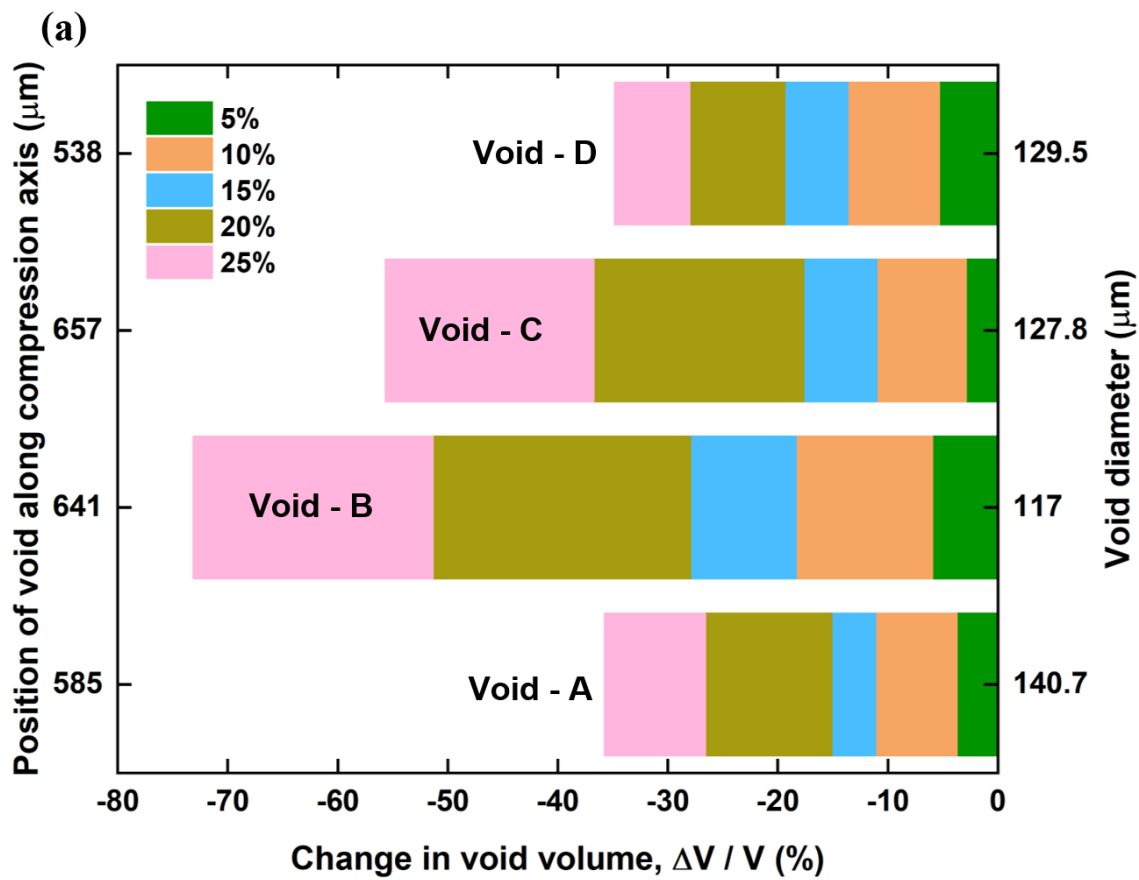


Figure 20: (a) Plot showing the changes in volume of four adjacent voids in increments of 5% strain. Position of the void from the contact surface and its size is also specified. (b) 3D rendering of the group of voids at multiple strain levels. Data and snapshot are of the marked-up voids in Figure 16 (a). Void A is not rendered for clarity. Regions within the dotted circles correspond to variation in cell-wall curvature and pre-buckled ligaments. White, red and yellow arrows point to same features marked in Figure 16 (a).

First by looking at both the ϵ_{xx} strain contours at 5% strain (Figure 21 (a)), we observe a strong positional effect of voids, i.e., ligaments and voids closer to the platen exhibit higher strain values. On examining this map closely, a diffused band of strained region, near the pre-buckled ligament (denoted by white arrow), to the left of void B is observed. This region is also experiencing a larger amount of lateral tensile strains (Figure 21 (b)) leading to the early collapse of void B at small applied strains. This behaviour was also understood from Figure 20 (a) and (b) showing the changes in void shape and volume. However, the complex heterogeneity in trends of the change in volumetric strain seen at $\epsilon=0.20$ in Figure 20 (a) can only be captured by DVC maps. From the ligament strain map along compression (ϵ_{xx}) shown in Figure 21 (c), we observed that the collapse of void B initiated the formation of a plastic hinge in the ligament between B-C (denoted by red arrow, also marked in Figure 16, Figure 20 (b)). This is exacerbated by the existing plastic hinge formed on the other side (denoted by the yellow arrow, also Figure 16, Figure 20 (b)) due to lower strength from the variation in cell-wall curvature. Under the developed bending moments, ligament between B-C rotated, inducing eccentricity and further strain to faster collapse. Thus, the heterogeneity in cell-wall strength dominated the onset and propagation of instable collapse over void size, shape and its position from the external

contact surface. This DVC approach was able to demonstrate the local behavior at the microscopic cell level at low strains. Extending this approach at large strains is more difficult since it will require an abundance of closely spaced markers and acquiring dynamic scans to capture the extreme changes in deformation. This is the subject of future work.

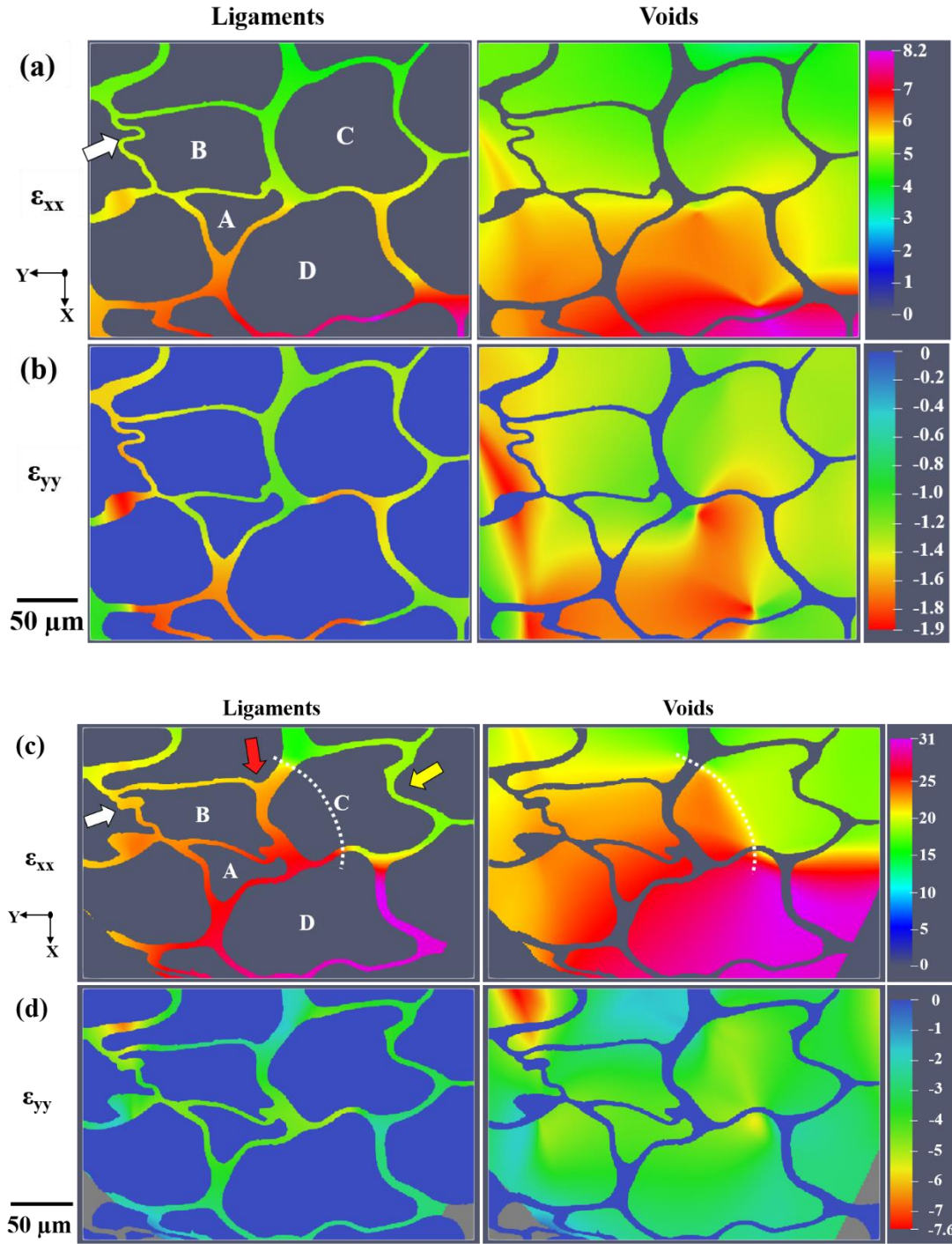


Figure 21: Strain maps (ϵ_{xx} , ϵ_{yy}) of the ROI in Fig.16 at an applied strain of (a)-(b) 5% and (c)-(d) 15%. Units of strain is percentage. Positive and negative values denote compression

and tension. Strain in the ligaments and voids are shown separately for clarity. White, red and yellow arrows point to same features in Figure 16 (a) and Figure 20 (b).

3.4 Conclusions

The deformation behaviour of ETPU bead foam used in footwear midsole under compression was studied using *in-situ* lab-scale X-ray microtomography. Strain maps were computed from image correlation on the time-resolved observations which elucidated the global and local mechanical response. The major findings of the study are:

- A correspondence between the morphological parameters and global deformation was obtained. The non-uniformly symmetric void size distribution coupled with increase in ligament thickness from the surface to the core of bead in 3D resulted in uniform contact stiffness near both platens and moderated the post-buckling behaviour.
- The proposed DVC approach by tracking voids to examine 4D datasets was adequate and established the link between cell structure changes at different locations within the bead with analytically computed strains.
- Strain mapping demonstrated that the heterogeneities in cellular structure around the immediate neighbours influenced the onset of local instability in void collapse rather than the position of void and its size in an ever-changing contact surface.

CHAPTER 4

MECHANISMS OF DEFORMATION IN eTPU MOLDED BEAD FOAMS IN COMPRESSION VIA *IN SITU* SYNCHROTRON X-RAY MICROTOMOGRAPHY

4.1 Introduction

Bead foams are multiscale materials that are used in a wide variety of engineering applications. Individual beads have a hierarchical cellular structure. The beads themselves are then bonded together to be used in service in a variety of applications such as bumper cores and bicycle helmets for impact protection [9, 17, 32]. Expanded thermoplastic polyurethane (eTPU) is used in midsoles of running shoes to improve energy return [68, 76].

One of the most commonly used material constants is the Poisson's ratio, an important parameter that quantified the compressibility of a material. Depending on the cellular structure, positive, negative, and a zero values of Poisson ratio have been reported [77–80]. Also, different definitions of Poisson's ratio exist depending on the material behavior and the state of deformation [77, 80–82]. For an elastic material, the ratio of lateral to axial engineering strains is used, whereas for materials strained to large deformations, stretch ratios (for viscoelastic materials) or true strains have been used in calculating the Poisson ratio. Rinde [80] measured the Poisson ratio for three low density foams (polystyrene bead (PSB), polyurethane and polypropylene foams) in tension and compression using the buoyancy technique, which measures volume change and is directly related to the strains. Sanborn et al. [77] studied the strain rate dependent nature of Poisson

ratio for silicone foam at quasi-static and dynamic strain rates. Radial strains were measured using a diametrical laser sensor and high-speed camera. RD Widdle Jr. et al. [83] estimated the Poisson ratio of a flexible polyurethane foam using digital photography in conjunction with image processing. These methods of identifying strains and Poisson ratio lacked information on the initial cellular structure and its change during the deformation. To overcome this, X-ray tomography can be used, which enables a time-resolved understanding of physical mechanisms under various conditions in three dimensions. However, the use of lab-scale CT for this problem is time consuming due to two reasons. Primarily, even in low X-ray attenuating materials, to get high contrast images longer scans are required due to the lower flux of the source (up to 14 h or more for one tomogram). Secondly, there is an extended wait time between scans after the sample is compressed to avoid image blurring from the residual motion due to stress relaxation. This can be avoided by the use of synchrotron x-rays where shorter scans are possible due to the high photon flux (~ 3-5 orders of magnitude higher than lab-based sources) [65]. Patterson et al. [65] used *in situ* compression using x-rays at Synchrotron to measure axial and radial deformation of hyperelastic silicone foams under quasi-static strain rates. They showed the change in Poisson ratio with compressive strain depends strongly on cell morphology.

From review of the literature it is evident that the determination of Poisson's ratio in foams requires simultaneous *in situ* measurements of 3D strains in the specimen. Digital volume correlation (DVC) is one such technique that enables calculation of strains at bulk or local scales. It is a 3D extension of digital image correlation (DIC) technique [84]. In order to perform DVC, one needs a digitized representation of the volume, which can be achieved through x-ray computed tomography (X-ray CT) [85]. Synchrotron X-ray sources

provide the best tool for studying the microstructural evolution volumetrically when 3D images must be acquired over short timescales. The combination of DVC on CT data has been used to understand damage evolution in additively manufactured polymer matrix composites, auxetic polyurethane foams, polypropylene, and thermoplastic polyurethane bead foams [18, 52, 85, 86]. By use of these tools, both a qualitative and quantitative understanding can be achieved in studying the complex mechanical behavior of cellular materials at relevant length scales.

The objective of this work is to investigate the bulk deformation of bead foams with varying cellular morphologies. *In situ* compression experiments were performed using synchrotron x-rays to capture the 4D behavior. An image processing workflow was developed to extract quantitative measurements of deformation and to relate these to the multiscale cellular structure in the material. DVC technique was used to measure the bulk strains. Finally, the dynamic 4D measurements enabled accurate measurement of the Poisson's ratio for the foams. The relationship between the Poisson's ratio and cellular structure is described and discussed.

4.2 Material and Methods

4.2.1 General overview of testing

Plates of eTPU were prepared by steam chest molding, i.e., the expanded TPU beads are injected into a plate mold (having dimensions 200 mm x 200 mm x 10 mm) wherein individual beads are fused by heat from steam and pressure. Two plates with a nominal density of 200 kg/m³ and 220 kg/m³, having different cellular structures were chosen. From the plates, cuboid-shaped samples approximately 15 x 15 x 10 mm were cut with a

sectioning knife at room temperature and the edges trimmed. This sample size ensured at least one full single bead was within the field of view, at optimal resolution to study the changes in cellular structure within the bead (see Figure 22 (b)) and at the interface between the beads.(see Figure 22 (c)). The optimal resolution was determined based on the feature of interest that needs to be studied and the volume of material within the FOV (based on detector size and sample size). Here such information on the range of ligament thicknesses, void sizes were obtained from lab-scale CT of beads. And at this chosen resolution, one would want to have enough material within the FOV during the experiment and collect meaningful data. Two samples from each plate were cut to study the deformation under a continuously applied compressive strain using *in situ* x-ray synchrotron microtomography. In addition to this, individual beads before fusion (from one plate type) were also compressed. A pictorial representation of the above is shown in Figure 22 (a).

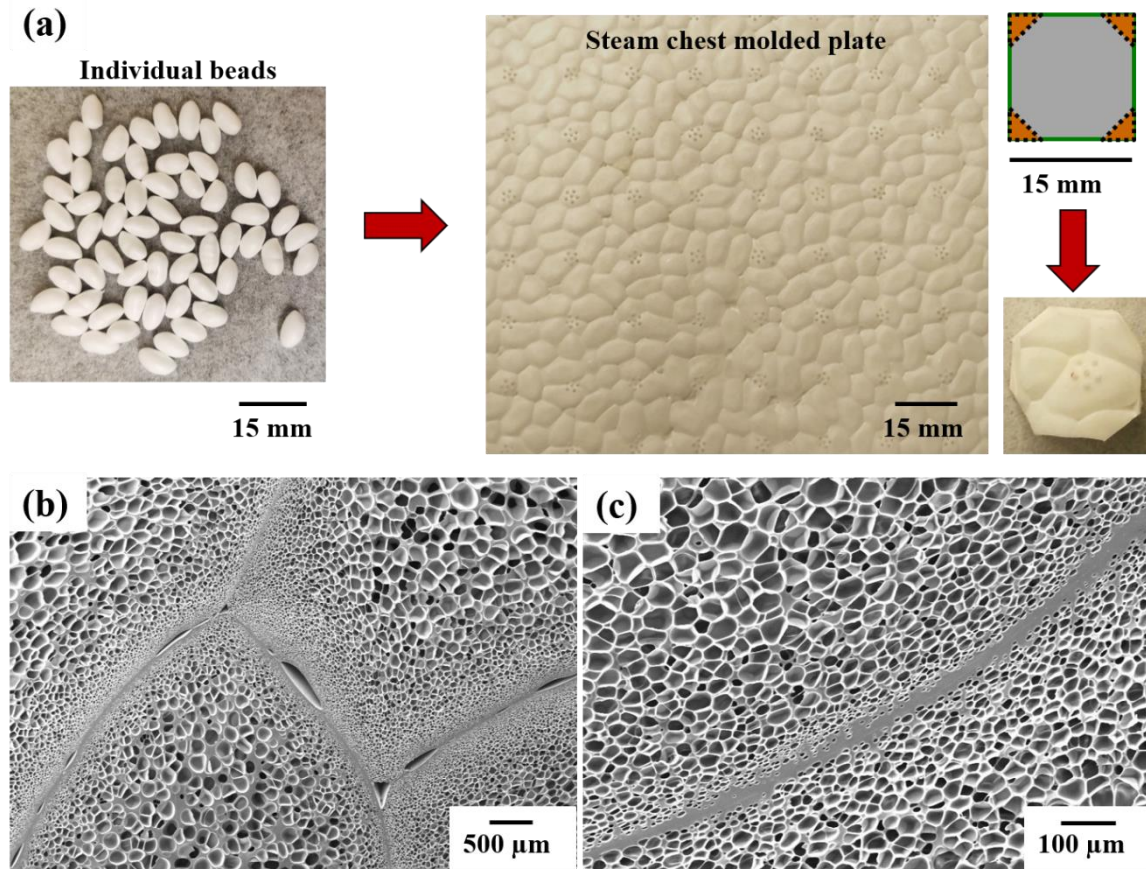


Figure 22: (a) Photographs of the samples used for testing, i.e., individual beads and molded plate samples. Scanning electron microscope image of (b) molded plate showing multiple bead interfaces and the cell structure within beads and (c) high magnification image of the interface.

4.2.2 *In situ* microtomography at the Advanced Photon Source (APS)

X-ray microtomography was performed at the Advanced Photon Source at the Argonne National Laboratory, Beamline 2-BM. A schematic of the experimental setup with loading fixture is provided in Figure 23. Details of the tomography setup have been described elsewhere [87, 88]. The experiments were done during continuous compression of the bead,

i.e., the experiment was not paused at all. Thus, the 3D scans had to be extremely fast, i.e., in the 1 s range. Typically, monochromatic beams are used in synchrotron to avoid the beam hardening effects present in polychromatic lab-source CT. However, the monochromator on a beamline, typically transmits less than 0.1% of the beam, reducing the flux and increasing the data collection times [89]. Since the scans were fast, a large flux in photons was required. With this in mind, the beamline was configured for polychromatic ‘pink’ beam imaging with a peak intensity at 24.9 keV. Herein, the monochromator is not used, and the x-ray beam is reflected from a grazing incident mirror. The mirror coating and angle determines the tunable energies. This high photon flux is more than 1000 times brighter than that of the monochromatic white beam and provided the necessary signal-to-noise ratio in the projections. High resolution x-ray imaging was accomplished using PCO Edge CMOS camera combined with 2x magnifying objective lens to provide isotropic voxels with a size of 2.1 μm . The tomographic field of view (FOV) measured was 2016 x 900 pixels, i.e., 4.4 mm in width and 1.9 m in height. Since the samples were larger than the full FOV, a vertical stitch scan was done with a 20% overlap to increase the data collected along the height of the sample. This was done by programming the vertical motion of the stage to move down (after the first scan) and move back up (after the second scan) as shown in Figure 23 (b). In this manner, a total FOV of 4.4 mm x 3.4 mm was scanned.

A vertical stitch scan was performed on the sample in its initial state, i.e., at zero strain. Dynamic x-ray microtomography was performed on the ETPU molded samples by a custom loading fixture shown in Figure 23 (a). This fixture has been previously detailed [90] and used for *in situ* compression studies at a synchrotron imaging beamline [65]. Tests

were conducted with a displacement rate of 0.001 mm s^{-1} , and this corresponded to a strain rate of $1 \times 10^{-4} \text{ s}^{-1}$ ($2 \times 10^{-4} \text{ s}^{-1}$ for beads). Vertical stitch scans were taken at regular intervals of every 2.7 % strain ($\sim 5.5 \%$ strain for beads) while the sample is undergoing compression (see Figure 23 (b)). In all the scans, 1,500 evenly spaced images were acquired over a 180° rotation range at a rotation rate of 30° s^{-1} with 0.5 ms exposure for each image. This combination of voxel size, time per scan and displacement rate meant that there was no image blurring during the acquisition of a full tomogram. In other words, a voxel only moved by a micrometer relative to the first projection before the full scan was completed. Since polymers are prone to x-ray damage, the effect of synchrotron x-rays on the plate samples were evaluated by compressing the samples both before and after exposure in a microforce testing machine. The compressive stiffness did not vary suggesting that the short (but high) x-ray dose did not significantly affect the mechanical properties.

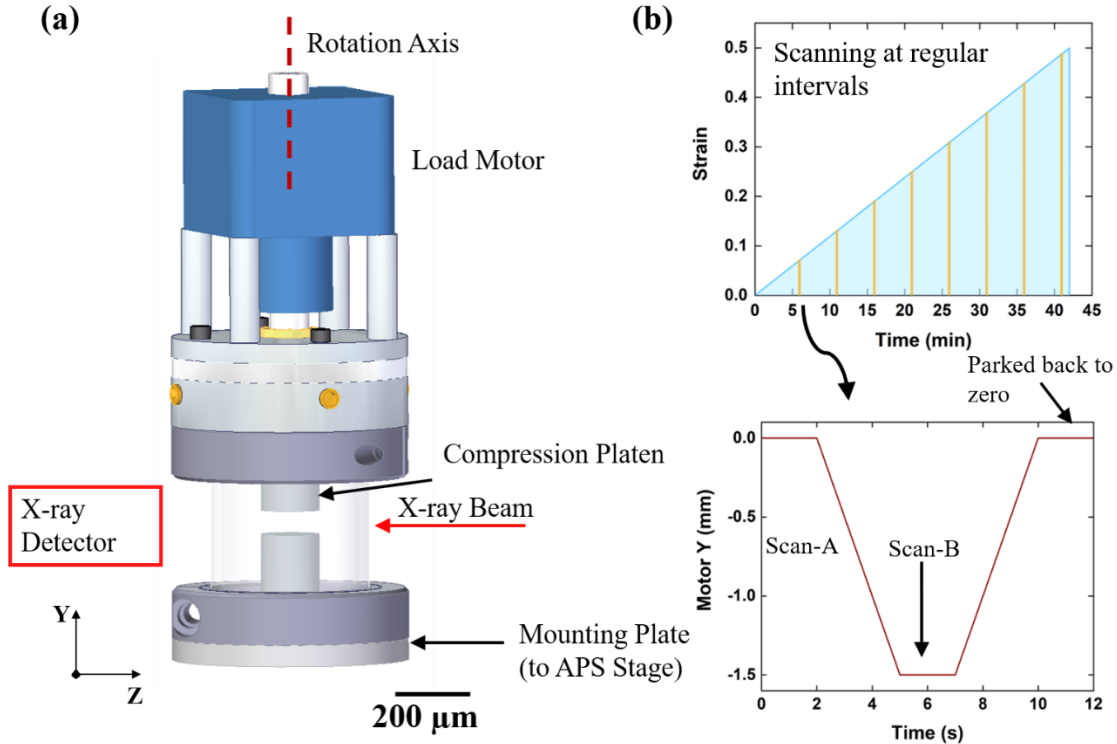


Figure 23: (a) Schematic of beamline and loading fixture layout for CT imaging with the *in situ* compression testing. (b) Plot of applied strain versus time showing the continuous straining and intermittent scans during which the motor Y is programmed to move to allow vertical stitched scans.

4.2.3 Image analysis

Sinogram images were processed using TomoPy [91] for GRIDREC reconstruction [92], using stripe removal filtering [93]. Post processing of the data was done in MATLAB R2018b[®], following a multistep process graphically shown in Figure 24. The stack of .tiff images was loaded as a 3D array and filtered using an edge-preserving smoothing / anisotropic diffusion filter, depending on the dataset, to smooth out noise. A simple grayscale threshold was used to obtain the binarized image of voids in which a “fill holes” algorithm was used. The fill holes algorithm is intended to close small holes within the voids that might be present due to image artifacts. This was subsequently eroded to remove the small objects, thereby saving time during the labelling process and to remove the narrow regions connecting clusters. These eroded voids were then quantified based on 3D connectivity of an object using an in-built function called `regionprops3`, which uses a flood-fill algorithm to label all the pixels in the connected component containing the unlabeled pixel, p . This process was repeated until all the pixels were labeled for quantification. An iterative process was then employed to label only voids which fell within the volume bounds. Those larger than the user specified limit meant that multiple voids were connected as a single island due to leaks during binarization. Such leaks are bound to happen since the ligaments and voids had very little difference in grayscale intensities (see Figure 25

(d)) and also due to thin ligaments in the foam wherein conventional binarization fails. These were then isolated and eroded, checked against volume and shape constraints, until there were no remaining islands having a volume larger than the set limit. In this manner, we converted the grayscale 3D data into a 3D array of labelled voids at each strain, which was then used for strain mapping.

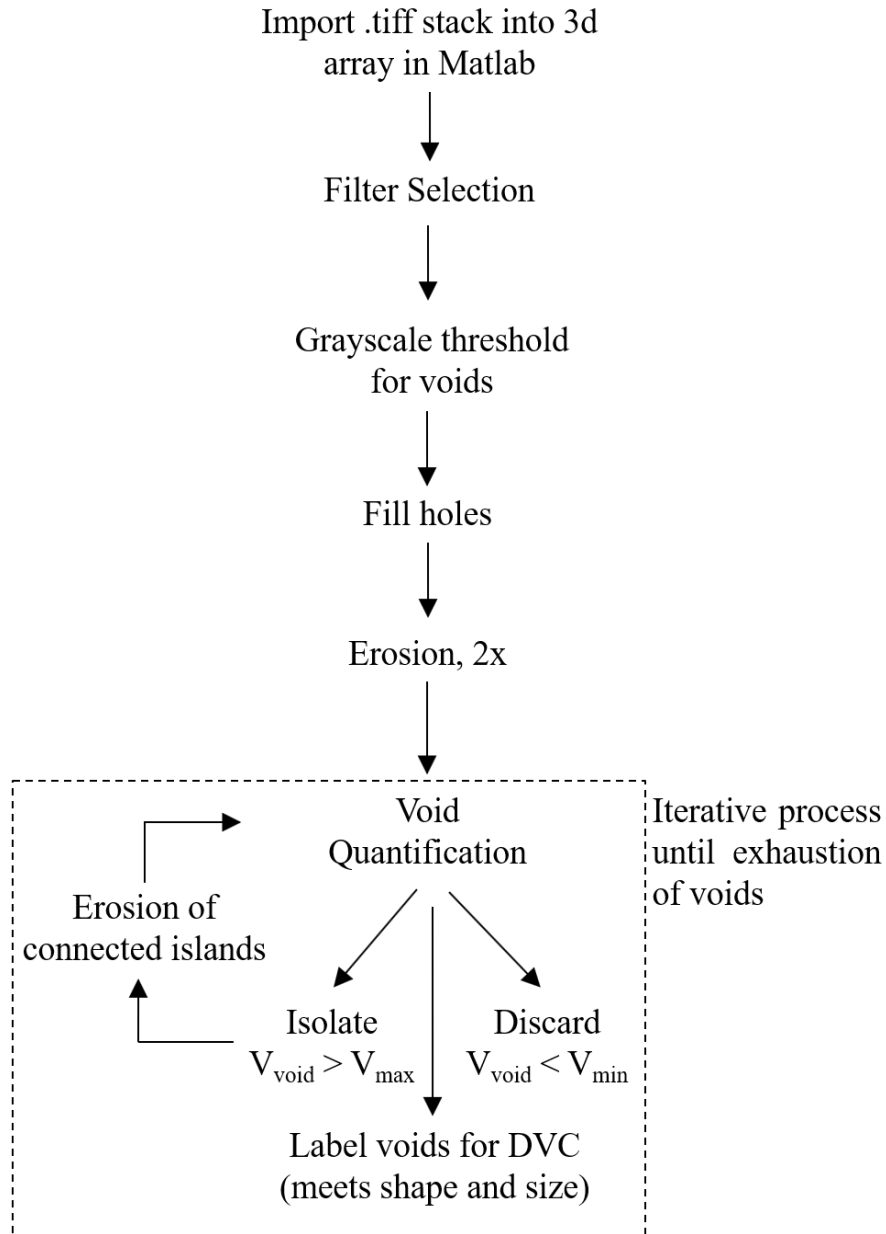
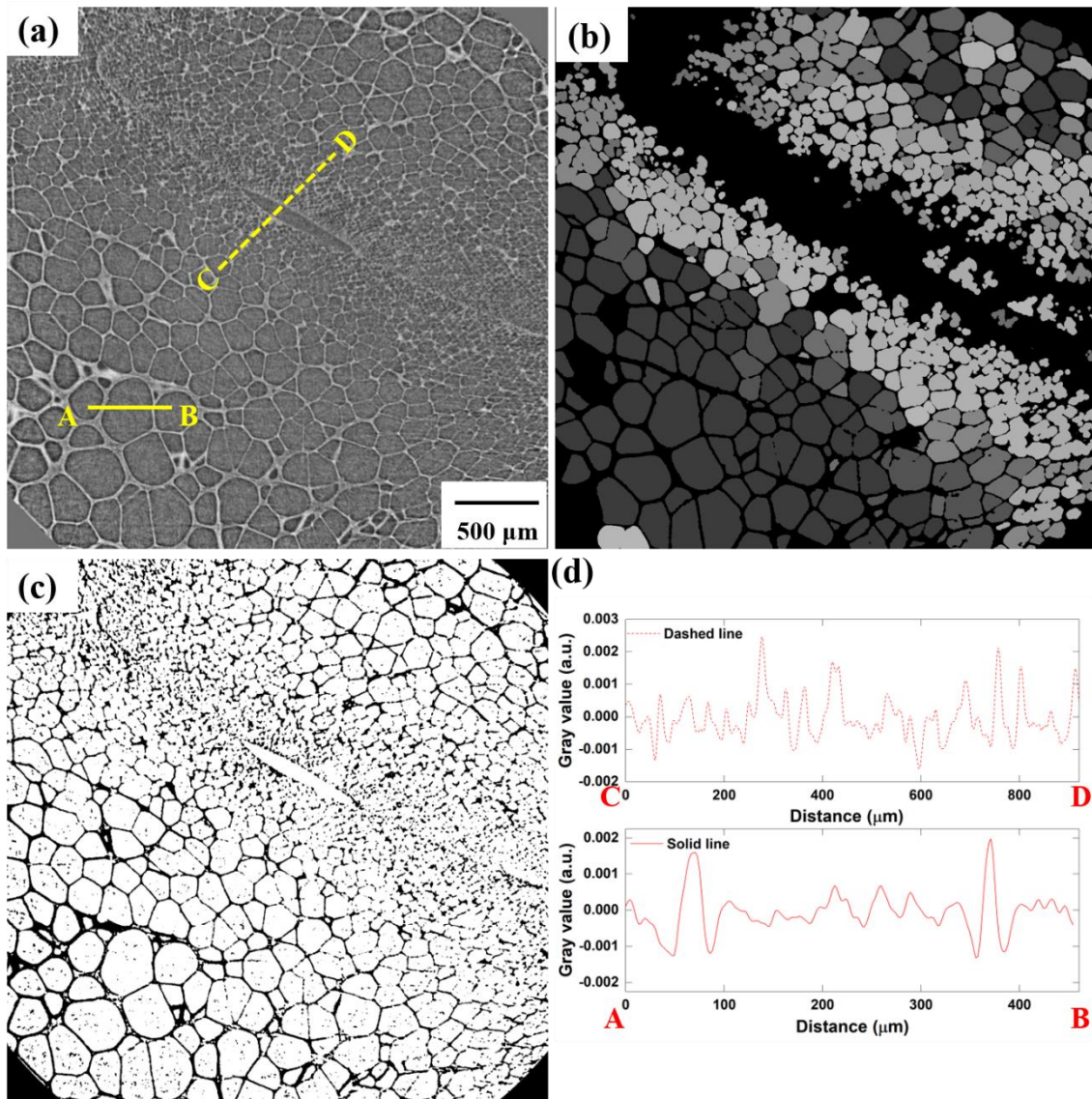


Figure 24: Flowchart of the process used in image segmentation, i.e., labelling voids. Process involves smoothing the data, isolating voids, and an iterative selection of voids based on size criterion.

The accuracy and validity of the iterative image analysis process is shown in Figure 25. Figure 25 (a) shows a 2d grayscale image of a molded plate at zero strain. Figure 25 (c) shows the segmented image based on conventional binarization. The threshold value was selected after analyzing several grayscale line profiles like the ones shown in Figure 25 (d), which shows very little difference in intensity between the ligament and voids. Looking at Figure 25 (c), we can see that conventional binarization leads to erroneous connectivity and the entire data is lumped as a single entity. This data was then processed using the image analysis routine. The final label field shown in Figure 25 (b) demonstrates the ability of the algorithm to identify the individual voids. The smaller voids at the bead interface in the label field in Figure 25 (b), were either missing or clustered as a larger void. Those missing voids were rejected since they were smaller than the image resolution. Clustered voids were not reported in void diameter distribution. The *in situ* datasets were then processed using the same user-defined inputs as in zero-strain. Figure 25 (e) shows the variation in total voids available for labelling versus the labelled voids at every iteration for three strain intervals including zero-strain. At the end of first iteration, there is a local minimum in the plot, indicating that only a few voids match the criterion and that the remaining portion of the image consists of clusters of neighboring voids touching each other due to the thin ligaments (leading to leaks in segmentation). With increasing iterations, a global maximum in the plot is seen, signifying that most of the void clusters have been separated. Eventually a global minimum is seen indicating that there are no

additional clusters available for labelling in the next iteration. The total number of voids labelled at the end of the iterative process is shown versus the respective time steps in the plot. The number of voids that was labelled through this self-exhaustive iterative process remains within a close range at various strains. Also, the curves showing the variation in identified voids versus labelled voids overlap for different strains. This shows that the algorithm can consistently identify voids in the same manner which gives us confidence in applying this routine to similar 4D datasets.



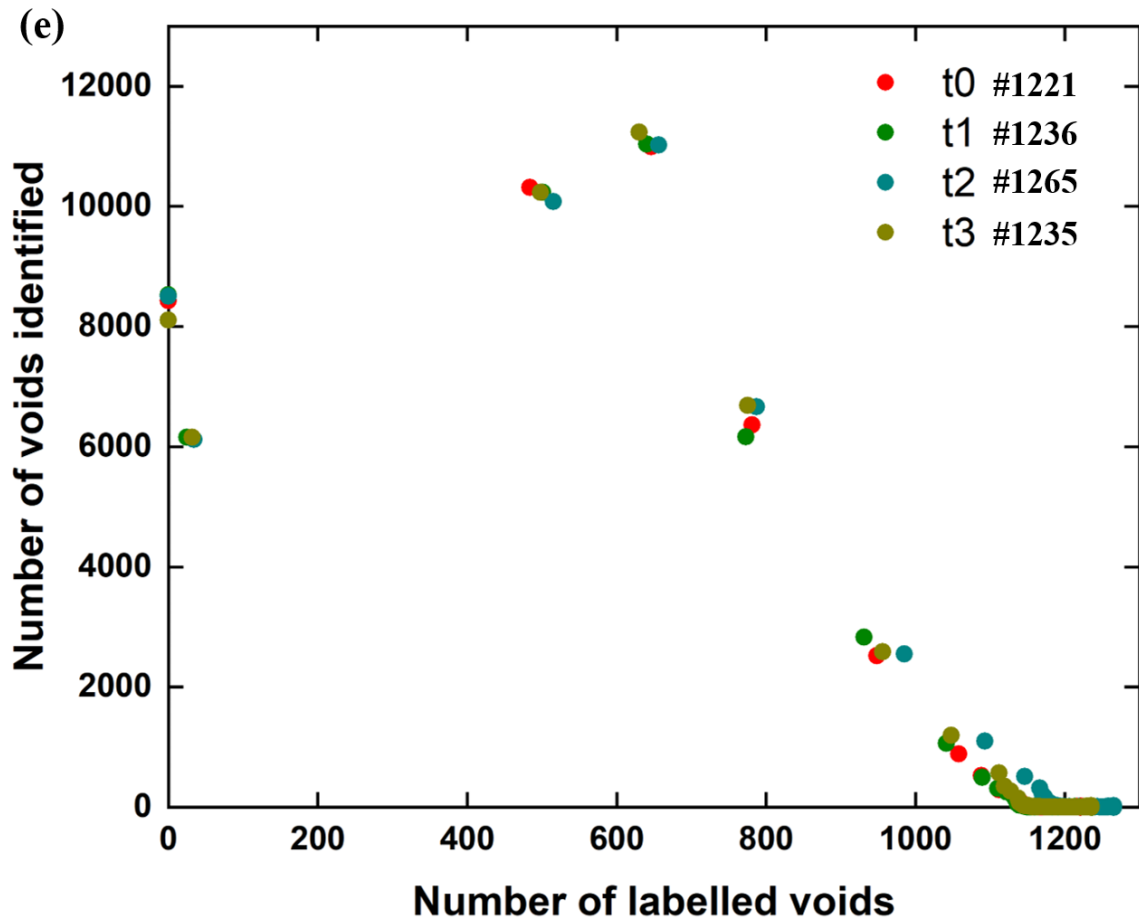


Figure 25: (a) Grayscale image of molded plate at zero strain from CT. (b) Labelled image of the same slice shown in (a) after image segmentation using algorithm in Figure 24. (c) Labelled image of the same slice shown in (a) after conventional thresholding. (d) Grayscale values of the lines marked in (a) showing the intensity variation between voids and ligaments. (e) Plot of voids identified and labelled at every iteration for three strain levels plus zero strain with final count indicated against strain state.

4.2.4 Estimating strains using DVC

The molded foams were imaged *in situ* at various points during compression, resulting in 4D datasets which were ideal for volumetric strain mapping through feature tracking. For

this purpose, the centroids of voids were tracked. An overview of the DVC method employed here has been previously described elsewhere [86]. The only difference in this work is the additional image processing after labelling the voids, which enabled full field of view (FOV) for calculating three-dimensional displacement field. In our case, since the voids are labelled automatically there is no guarantee that the same voids were identified in all the datasets. Also, the void labelling doesn't necessarily have to follow the same order. To ensure a one-to-one correspondence in the voids at all time stamps, a k-nearest neighbor search was done based on position at a given applied strain. First, the centroids of the preceding strain (data1) were moved along the axis of compression by the strained value. Then, for each centroid in the succeeding strain (data2), one nearest neighbor in the modified preceding strain (data1) was found per the following syntax:

$$[idx] = knnsearch (centroid_{data2}, centroid_{data1}, 'K', 1, 'Distance', 'euclidean') \quad (5)$$

Once the indices (*idx*'s) of the match were found, a size match was conducted and the voids re-numbered in the same sequence. The criteria involved examining the change in volume of the matched voids. Thereafter, the displacement fields were calculated and converted to a strain field for the three primary volume directions (ϵ_{xx} , ϵ_{yy} , ϵ_{zz}). The loading direction, which was parallel to the compression axis, defined here as being parallel to ϵ_{xx} .

4.3. Results

4.3.1 Morphological Characteristics

As mentioned earlier, molded plates with varying cellular structure were studied. Figure 26 shows the stitched virtual CT slices of samples with a radial variation / gradient in

cellular structure in the individual beads and molded plates prepared using these beads at zero strain. The stitch is clearly noticeable in Figure 26 (b) by a split in grayscale intensity between the halves. The direction of compression is top down in the plane of the figure. The position of the largest ligament is marked through a dashed circle in the different samples. The individual beads with a graded structure and molded plates prepared using them are abbreviated as BG and PG respectively. BG1, BG2, PG1 and PG2 refers to the sample imaged at synchrotron under continuous compression. BG3-l (full field of view low resolution data) and BG4-h (high resolution data of skin region, near the compression platens) refers to samples compressed using lab-scale CT in an interrupted *in situ* modality. These microstructures shown in Figure 26 are characteristic of the vessel expansion process and are described in detail in Section 3.3.1.

The other set of microstructures investigated had a homogeneous distribution of cells and ligaments and is shown in Figure 27. Figure 27 shows the CT slice of the homogeneous cellular structure bead and a molded plate prepared using them. The individual bead sample was imaged using lab CT for quantification only, i.e., no compression experiments were carried out.

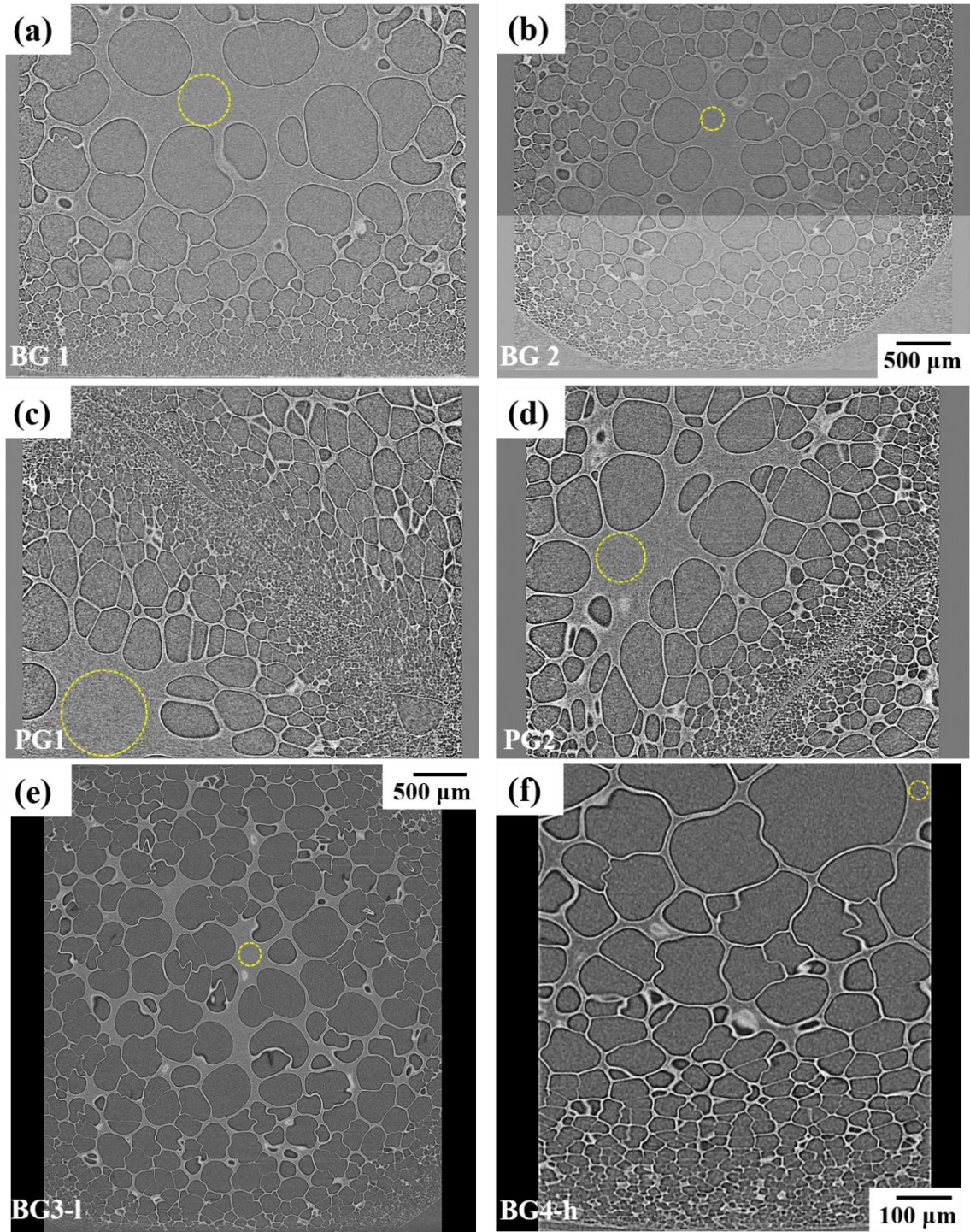


Figure 26: X-ray CT slice of samples before compression at zero strain. (a) and (b) Individual beads with graded cell structure. (c) and (d) Molded plates from graded beads.

(e) and (f) Individuals beads with graded cell structure compressed using lab scale CT. ROI in (f) is limited to region near the platen. BG- bead graded, PG-plate graded, BG-h-bead graded high resolution. Dashed circle represents the largest ligament size.

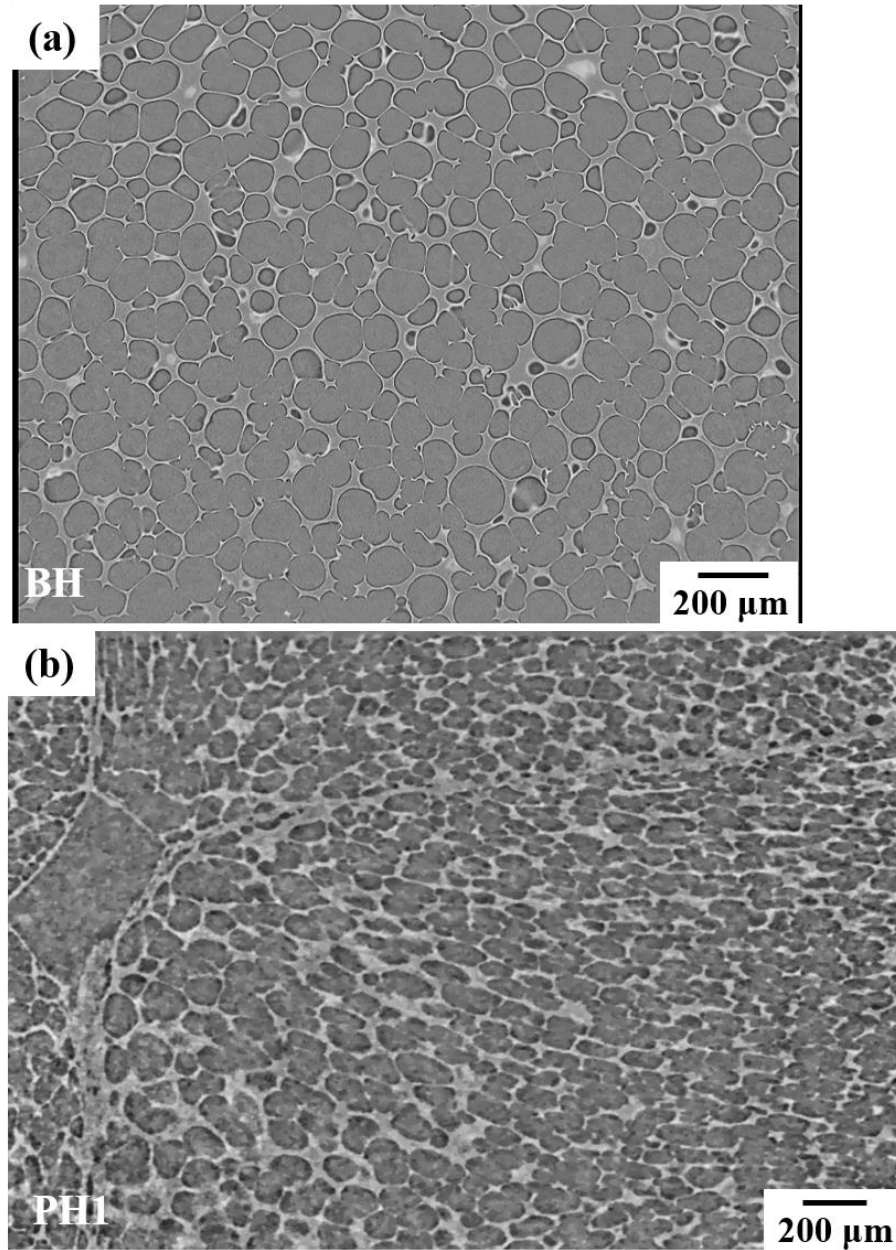


Figure 27: X-ray CT slice of samples at zero strain with homogeneous cellular structure. (a) Individual bead. (b) Molded plate. BH – bead homogeneous, PH – plate homogeneous.

Figure 28 shows the ligament thickness and void size distribution in the individual beads and molded plates. The position of the largest ligament is marked by a dashed circle in Figure 26. These calculations were done on the zero-strain data, which can help in elucidating the deformation behavior, in turn the Poisson ratio. Void size is represented as the diameter of a sphere of equivalent void volume, while the ligament thickness is computed from the maxima of 3D distance map. On observing Figure 28 (a) and (b), we notice that there is variability in the microstructure obtained from the same batch of material foamed using vessel expansion technique. This could be a result of the differences in local changes in temperature and pressure profile the bead experiences during the foaming. Moreover, the variability could alter the void channels that form at the bead to bead interface when these are pressed against each other in the mold before steam chest process due to differences in stiffness. This requires further investigation by carrying out *in situ* molding trials. On the other hand, these parameters on the plates with homogenous cellular structure weren't quantified, since the features were below the resolution to have useful information. Instead, lab scale CT scan of an individual homogenous bead shown in Figure 27 (a) was used for quantification and data is shown in Figure 28 (e) and (f). Though only a single bead (with homogeneous structure) was quantified, the distribution of ligament thickness and void size is narrow. Table 3 summarizes the ligament thickness and void size distributions seen in Figure 28.

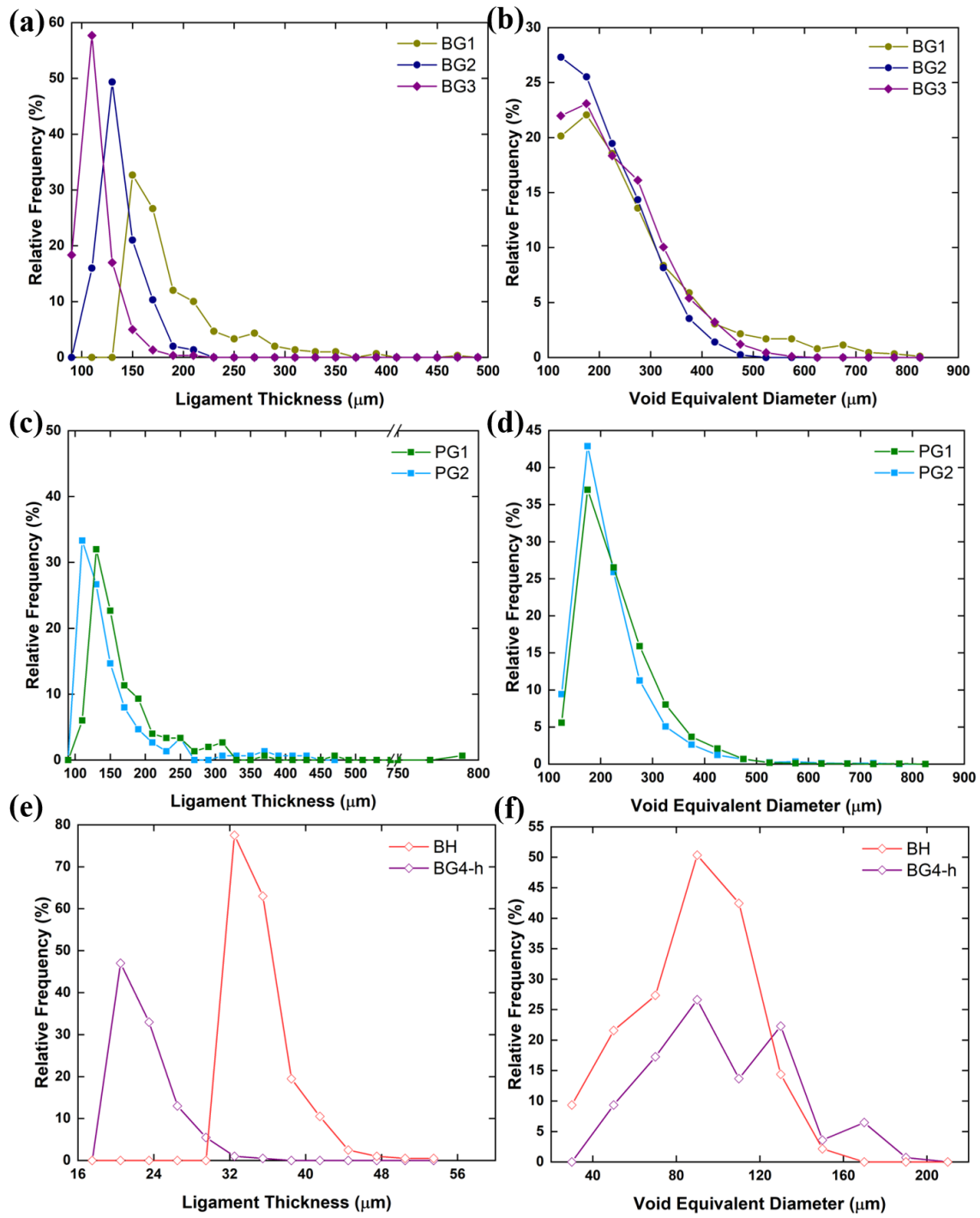


Figure 28: Relative frequency distributions of the ligament thickness (a, c, e) and void equivalent diameter (b, d, f) of the samples. (a) and (b) are for individuals beads with graded cell structure (BG). (c) and (d) are for molded plates from graded beads (PG).

Table 3 Details of the void size and ligament thickness distributions shown in Figure 28.

Sample	Void Equivalent Diameter (μm)			Ligament Thickness (μm)		
	# observations	Max	Average (S.D)	# observations	Max	Average (S.D)
BG1	884	817	253 (128)	300	469	189 (50)
BG2	2425	497	209 (75)		208	138 (19)
BG3	3553	578	228 (88)		213	113 (16)
PG2	2129	739	216 (74)	150	450	172 (63)
PG1	1716	755	230 (73)		780	171 (74)
BG4-h	139	188	103 (34)	200	34	23 (3)
BH-1	233	147	87 (27)		53	37 (3)

Figure 29 shows the CT slice of the two types of molded plate before compression and at 22% strain. In both the plates, cells walls in the beads have buckled, whereas the bead interfaces don't show any sign of buckling. The onset of densification of the interfacial voids between beads is seen in both the plates. The transition to buckling of bead walls in these foams are beyond the investigated strain.

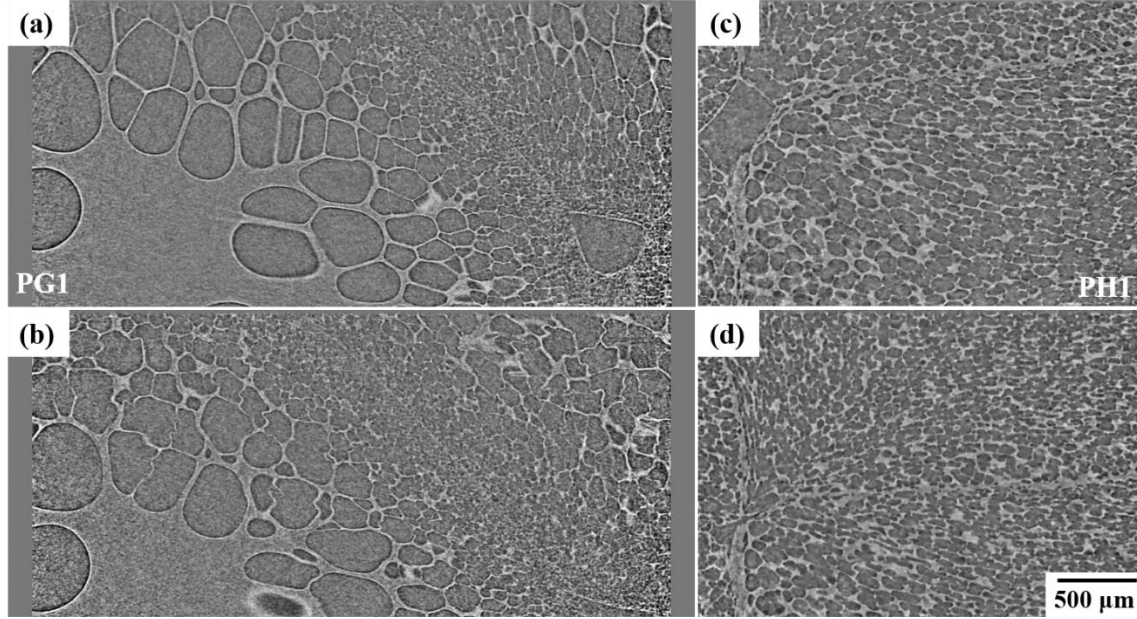


Figure 29: X-ray CT slice of molded plate samples before compression and at an applied compressive strain of 22%. a and c Zero strain. b and d 22% strain. PG – plate graded, PH – plate homogeneous.

4.3.2 Poisson's ratio

Figure 30 (a) shows the variation in the volumetric strain with respect to the observed compressive strain for both the individual beads and molded plates with graded microstructures. A similar plot showing both the types of molded plates, i.e., beads of homogeneous and graded cellular structure is shown in Figure 30 (b). Both the volumetric strain and compressive strain was calculated from the DVC analysis of *in situ* datasets. The calculated volumetric strain is defined as:

$$\frac{\Delta V}{V} = (1 + \varepsilon_{xx})(1 + \varepsilon_{yy})(1 + \varepsilon_{zz}) - 1 \quad (6)$$

where ε_{xx} , ε_{yy} , ε_{zz} are strains in the primary volume direction.

According to classical elastic theory, Poisson's ratio (ν) is defined as the negative ratio of the lateral strain to axial strain,

$$\nu = -\varepsilon_{yy}/\varepsilon_{xx} \quad (7)$$

$$\nu = -\varepsilon_{zz}/\varepsilon_{xx} \quad (8)$$

Equations (7) and (8) are substituted into eq. (6); and after rearranging the terms, the required equation relating volume change and poisson ratio is obtained:

$$\frac{\Delta V}{V} = (1 - 2\nu)\varepsilon_{xx} + (\nu^2 - 2\nu)\varepsilon_{xx}^2 + \nu^2\varepsilon_{xx}^3 \quad (9)$$

Figure 30 shows plots of calculated volumetric strain, from the tomography data, versus applied strain. Best fits of the data based on eq. (9), corresponding to a given Poisson ratio, were superimposed over the data. The upper and lower bounds in Poisson ratio, given by 0 and 0.5, are also shown.

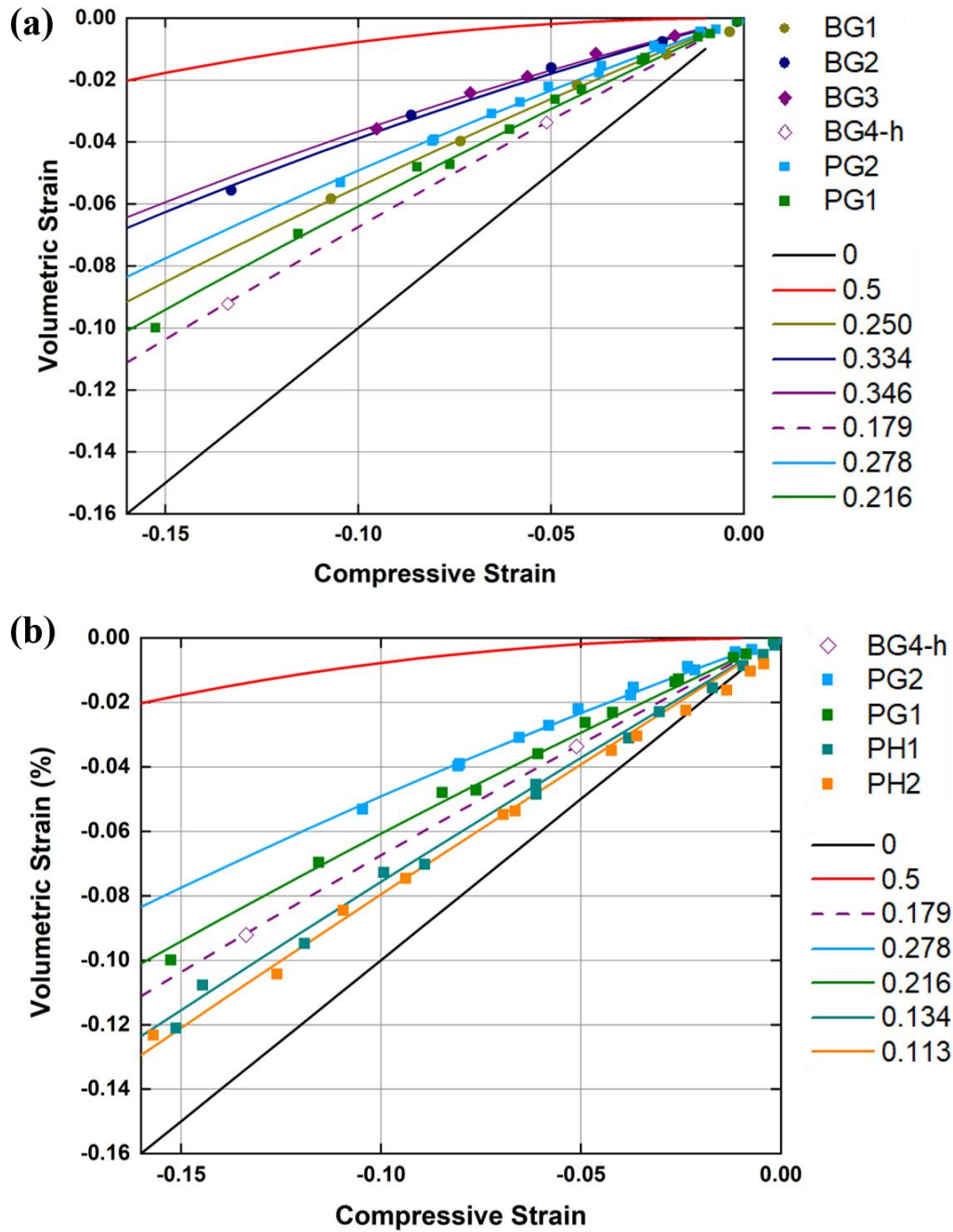


Figure 30: Plot showing the variation in volumetric strain against the compressive strain of the bead foam samples. (a) Graded individual beads and molded plates from graded beads. (b) Molded plates from homogeneous and graded beads. Symbols indicate experimental data from DVC. Solid lines represent poisson ratio calculated based on eq. (9).

4.4 Discussion

From Figure 26 (a)–(d) and Figure 28 (a)–(d), we notice that the individual beads with graded cell structure and molded plates prepared using these beads show a strong variation in both the void size and ligament thickness. These morphological variations present in the microstructure are known to affect the deformation behavior in conventional foams. Previous work through Laguerre tessellation by Chen et al.[94] also showed that these variations lead to an increase in dispersion of buckling of cell walls. This can be explained using the schematic in Figure 31. Here, we consider the ligaments in the foam as elastic springs with stiffness proportional to their thickness. For simplicity, the length of ligaments is the same, and bending and stretching are not considered. This scenario is shown in Figure 31 and has a total of 10 springs connected in series (of which only five are shown due to symmetry). The load applied is uniform across each spring in the case of series connection and the displacement is dependent on the stiffness of the spring. Since there is an increasing ligament thickness as one moves from the skin to the core, spring stiffness is represented in a similar fashion. This setup then leads to a larger displacement in the lower stiffness spring and smaller displacement in the stiffer spring. This is quite analogous to our case of beads with graded structures. In other words, one expects to see the thinner ligaments to buckle sooner and the thicker ligaments to yield at higher strains. This will lead to localization of strains in regions having thinner ligaments.

This identical behavior is seen in individual bead foams on comparing the 2D slices of individual beads BG-1 and BG-2 shown in Figure 32, taken at the same applied strain of ~28%. There is extensive densification near the skin or region of contact in both BG-1

and BG-2, where the smaller cells and thinner ligaments are present. However, buckling of ligaments is seen more uniformly in BG-2 compared to that of BG-1. This is due to smaller variability in ligament thickness and a lower mean thickness in BG-2 compared to that of BG-1 (see Table 3). It is also evident that the thicker ligament in the central region in BG-1 are yet to buckle, i.e., stronger. These ligaments lead to preferential densification in the weaker regions and strengthening in the central core.

The compression experiment carried out on individual beads is like an elastic sphere being compressed between two rigid plates and naturally tends to expand laterally. This lateral expansion is affected by the deformability of the structure. Consider the case of BG-1, where there is strengthening from thicker ligaments and localization of densification near the platens. There is an increased resistance to the progress of deformation zone towards the central region. This is reflected by the lower Poisson ratio of this bead (see Figure 30 (a)). However, in BG-2 and BG-3 the ligament distributions are smoother with an average thickness 30% and 40% lower than that of BG-1. With increasing strain, ligament buckling continues and the damage zone progresses inwards due to the absence of constraint in the central core. This leads to a larger lateral extension at the free surface of the bead and a higher Poisson ratio (see Figure 30 (a)). This dependence of Poisson ratio on the initial microstructure of beads is also seen in the presence of constraint, i.e., in molded plate form (see Figure 30 (a)). Both plates, PG-1 and PG-2, have similar distribution of cells as well as average ligament thickness but have very different maxima as seen in Figure 28 (c) and Table 3. A similar behavior, as explained in the case of the beads, is expected in terms of strengthening (or increased resistance to buckling) from thicker ligaments and strain localization at weaker regions. PG-1 exhibits a larger value of

Poisson ratio compared to PG-2. Interestingly, the correlation gets stronger comparing BG-1 (bead with a free surface and point loading) and PG-2 (bead with constraint from surrounding cells and far-field uniform load). The maxima (449 μm and 469 μm) and the 80th percentile (192 μm and 214 μm) of ligament are higher for BG-1 than that of PG-2 and hence exhibit more volumetric strain overall.

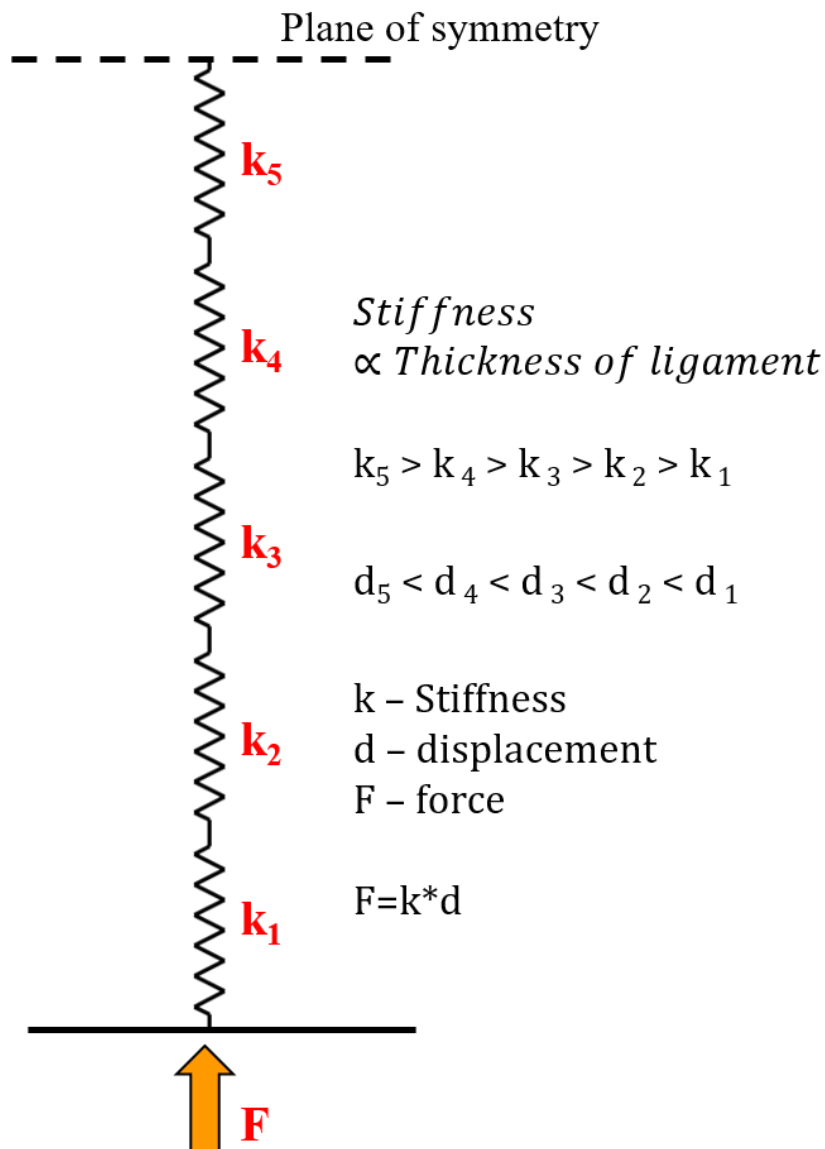


Figure 31: Schematic of springs connected in series used to explain the variation in strains due to varying ligament thickness in foams.

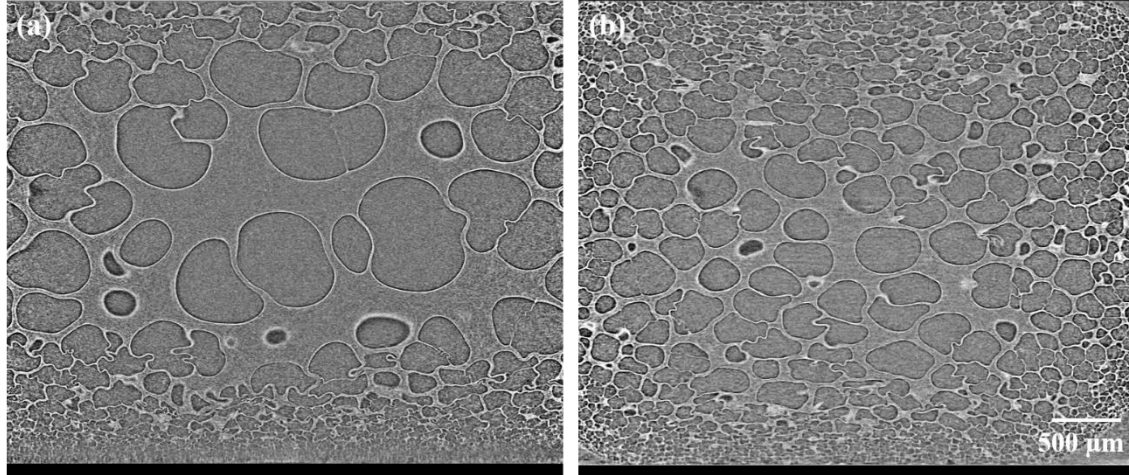


Figure 32: X-ray CT slice of bead samples at an applied compressive strain of 28%. (a) BG-1 (b) BG-2.

Figure 30 (b) shows a comparison of the Poisson ratio of molded plates with individual beads having a radial variation and an absence of variation in cell size and ligament thickness. As expected, the molded plates with homogeneous cell structures exhibited a lower poisson ratio. An analogy of ligaments in the foam to be an elastic spring can be used to explain the above (see Figure 31). The homogenous cell structure is an array of springs of similar stiffness throughout the entire volume. The resistance to deformation is uniform and the same at any given location. Now, the beads with a radial variation in ligament thickness can be thought of an array of springs, with stiffness proportional to thickness and varying with position. The resistance to deformation is non-uniform and location specific due to the varying spring stiffnesses. From Figure 28 (a), (c) and (e) and Table 3, we see that the ligaments in the beads used for PH plates are at least 5 times thinner than those of the beads with a radial variation. This difference translates to ligament buckling being initiated at lower strains. Combining this with the uniform distribution of

ligaments, we have a structure susceptible to more volumetric compression compared to those with a radial variation in features.

4.5 Conclusions

The bulk deformation behaviour of eTPU bead foam with varying cellular morphologies under compression was studied using *in situ* Synchrotron x-ray microtomography. An image processing workflow was developed to extract useful morphological characteristics and support to provide input data for DVC analysis. DVC on the time-resolved observations elucidated the global mechanical response. A correspondence between the morphological parameters and global deformation was obtained. The local stress state gets affected by the variation in material distribution which dominate the response of these foams. This translates into a strong correlation of poisson ratio and distribution of ligament thickness in foams.

CHAPTER 5

CONCLUSIONS

5.1 Summary of Research Findings:

- *In situ* interrupted compression through lab-based X-ray tomography helped in understanding the global and local deformation behavior of eTPU foam used in the midsole footwear. The radial variation in voids size, coupled with the increase in ligament thickness from the surface to core of the bead led to the moderation of post-buckling behavior. For the first time, this structure was visualized and quantified in 3D. Moreover, a DVC approach by tracking voids was developed and used to study the 4D datasets. Strain mapping demonstrated the integral role played by the microstructural heterogeneities in a cellular structure. They influenced the onset of local instability in void collapse rather than the position of void and its size in an ever-changing contact surface.
- Quasi-static *in situ* Synchrotron X-ray microtomography helped in elucidating the role of cellular morphology in altering the bulk deformation of eTPU bead foams under compression. An image processing workflow was developed to extract useful morphological characteristics and to provide input data for DVC analysis. DVC on the time-resolved observations was used to obtain Poisson ratio of foams. The local stress state in these foams get affected by the variation in material distribution which dominate the compressive response. This translates into a strong correlation of poisson ratio and distribution of ligament thickness in foams, i.e., a bead foam having a strong variation with thicker ligaments in core has a lower poisson ratio.

5.2 Future Work

The structure property relationship of eTPU bead foams studied through 4D X-ray tomography provided some very interesting results on the local deformation behavior at the microscale during compression. However, several authors have shown the importance of thermal history and crystallinity on the mechanical properties of thermoplastics. Even in our case, the investigated bead foams displayed very different hysteretic losses. Hence for future work, the influence of foaming on the nanoscale structure and their subsequent effect on the micro mechanical properties could lead to a process-structure-property relationship. With the advancements in plastic molding technology, another area to explore is the preparation of composite bead foams, i.e., mixing beads with varying cellular structure. The methodology outlined in Chapter 4 can classify Poisson ratio, which can then be used to optimize the different combinations in finite element models to achieve the desired mechanical response macroscopically. Also, this approach could lead to a molded bead foam with lesser interfacial voids between beads and identify potentially weak mesoscale regions in the design stage.

REFERENCES

1. Raps D, Hossieny N, Park CB, Altstädt V (2015) Past and present developments in polymer bead foams and bead foaming technology. *Polymer (Guildf)* 56:5–19. <https://doi.org/10.1016/j.polymer.2014.10.078>
2. Prissok F, Braun F (2010) US_2010_0222442_A1-Foams Based On Thermoplastic Polyurethanes-Patent
3. Guo Y, Hossieny N, Chu RKM, et al (2013) Critical processing parameters for foamed bead manufacturing in a lab-scale autoclave system. *Chem Eng J* 214:180–188. <https://doi.org/10.1016/j.cej.2012.10.043>
4. Köppl T, Raps D, Altstädt V (2014) E-PBT—Bead foaming of poly(butylene terephthalate) by underwater pelletizing. *J Cell Plast* 50:475–487. <https://doi.org/10.1177/0021955X14528524>
5. Nofar M, Ameli A, Park CB (2015) A novel technology to manufacture biodegradable polylactide bead foam products. *Mater Des* 83:413–421. <https://doi.org/10.1016/j.matdes.2015.06.052>
6. Nofar M, Ameli A, Park CB (2015) Development of polylactide bead foams with double crystal melting peaks. *Polymer (Guildf)* 69:83–94. <https://doi.org/10.1016/j.polymer.2015.05.048>
7. Standau T, Hädelt B, Schreier P, Altstädt V (2018) Development of a Bead Foam from an Engineering Polymer with Addition of Chain Extender: Expanded Polybutylene Terephthalate. *Ind Eng Chem Res* 57:17170–17176. <https://doi.org/10.1021/acs.iecr.8b04799>
8. Zhai W, Kim Y-W, Jung DW, Park CB (2011) Steam-Chest Molding of Expanded Polypropylene Foams. 2. Mechanism of Interbead Bonding. *Ind Eng Chem Res* 50:5523–5531. <https://doi.org/10.1021/ie101753w>
9. Hossieny N, Ameli A, Park CB (2013) Characterization of Expanded Polypropylene Bead Foams with Modified Steam-Chest Molding. *Ind Eng Chem Res* 52:8236–8247. <https://doi.org/10.1021/ie400734j>
10. Ge C, Ren Q, Wang S, et al (2017) Steam-chest molding of expanded thermoplastic polyurethane bead foams and their mechanical properties. *Chem Eng Sci* 174:337–346. <https://doi.org/10.1016/j.ces.2017.09.011>
11. Viot P, Bernard D, Plougonven E (2007) Polymeric foam deformation under dynamic loading by the use of the microtomographic technique. *J Mater Sci* 42:7202–7213. <https://doi.org/10.1007/s10853-006-1422-8>

12. Bouix R, Viot P, Lataillade J-L (2009) Polypropylene foam behaviour under dynamic loadings: Strain rate, density and microstructure effects. *Int J Impact Eng* 36:329–342. <https://doi.org/10.1016/j.ijimpeng.2007.11.007>
13. Cronin DS, Ouellet S (2016) Low density polyethylene, expanded polystyrene and expanded polypropylene: Strain rate and size effects on mechanical properties. *Polym Test* 53:40–50. <https://doi.org/10.1016/j.polymertesting.2016.04.018>
14. Mills NJ GA (1999) Shear and compressive impact of polypropylene bead foam. *Cell Polym* 18:157–74
15. Mills NJ, Moosa ASI (1999) Impacts of Hemispherical Strikers on Polystyrene Bead Foam. *J Cell Plast* 35:289–310. <https://doi.org/10.1177/0021955X9903500402>
16. Masso Moreu Y, Mills NJ (2004) Rapid hydrostatic compression of low-density polymeric foams. *Polym Test* 23:313–322. <https://doi.org/10.1016/j.polymertesting.2003.07.002>
17. Viot P, Plougonven E, Bernard D (2008) Microtomography on polypropylene foam under dynamic loading: 3D analysis of bead morphology evolution. *Compos Part A Appl Sci Manuf* 39:1266–1281. <https://doi.org/10.1016/j.compositesa.2007.11.014>
18. Roux S, Hild F, Viot P, Bernard D (2008) Three-dimensional image correlation from X-ray computed tomography of solid foam. *Compos Part A Appl Sci Manuf* 39:1253–1265. <https://doi.org/10.1016/j.compositesa.2007.11.011>
19. Pedrazzoli D, Manas-Zloczower I (2016) Understanding phase separation and morphology in thermoplastic polyurethanes nanocomposites. *Polymer (Guildf)* 90:256–263. <https://doi.org/10.1016/j.polymer.2016.03.022>
20. Yilgör I, Yilgör E, Wilkes GL (2015) Critical parameters in designing segmented polyurethanes and their effect on morphology and properties: A comprehensive review. *Polymer (Guildf)* 58:A1–A36. <https://doi.org/10.1016/j.polymer.2014.12.014>
21. Hossieny NJ, Barzegari MR, Nofar M, et al (2014) Crystallization of hard segment domains with the presence of butane for microcellular thermoplastic polyurethane foams. *Polymer (Guildf)* 55:651–662. <https://doi.org/10.1016/j.polymer.2013.12.028>
22. Cooper SL, Tobolsky A V. (1966) Properties of linear elastomeric polyurethanes. *J Appl Polym Sci* 10:1837–1844. <https://doi.org/10.1002/app.1966.070101204>

23. Hossieny N (2014) Development of Expanded Thermoplastic Polyurethane Bead Foams and Their Sintering Mechanism. University of Toronto
24. Begenir A, Michielsen S, Pourdeyhimi B (2009) Crystallization behavior of elastomeric block copolymers: Thermoplastic polyurethane and polyether- block - amide. *J Appl Polym Sci* 111:1246–1256. <https://doi.org/10.1002/app.29082>
25. Leung LM, Koberstein JT (1986) DSC annealing study of microphase separation and multiple endothermic behavior in polyether-based polyurethane block copolymers. *Macromolecules* 19:706–713. <https://doi.org/10.1021/ma00157a038>
26. Schneider NS, Sung CSP, Matton RW, Illinger JL (1975) Thermal Transition Behavior of Polyurethanes Based on Toluene Diisocyanate. *Macromolecules* 8:62–67. <https://doi.org/10.1021/ma60043a014>
27. Seymour RW, Cooper SL (1973) Thermal Analysis of Polyurethane Block Polymers. *Macromolecules* 6:48–53. <https://doi.org/10.1021/ma60031a008>
28. Clough SB, Schneider NS, King AO (1968) Small-angle X-Ray scattering from polyurethane elastomers. *J Macromol Sci Part B* 2:641–648. <https://doi.org/10.1080/00222346808212463>
29. Koberstein JT, Russell TP (1986) Simultaneous SAXS-DSC study of multiple endothermic behavior in polyether-based polyurethane block copolymers. *Macromolecules* 19:714–720. <https://doi.org/10.1021/ma00157a039>
30. Sui T, Salvati E, Zhang H, et al (2019) Multiscale synchrotron scattering studies of the temperature-dependent changes in the structure and deformation response of a thermoplastic polyurethane elastomer. *Mater Today Adv* 4:100024. <https://doi.org/10.1016/j.mtadv.2019.100024>
31. Yanagihara Y, Osaka N, Iimori S, et al (2015) Relationship between modulus and structure of annealed thermoplastic polyurethane. *Mater Today Commun* 2:e9–e15. <https://doi.org/10.1016/j.mtcomm.2014.10.001>
32. Mills N, Fitzgerald C, Gilchrist A, Verdejo R (2003) Polymer foams for personal protection: cushions, shoes and helmets. *Compos Sci Technol* 63:2389–2400. [https://doi.org/10.1016/S0266-3538\(03\)00272-0](https://doi.org/10.1016/S0266-3538(03)00272-0)
33. Barzegari MR, Hossieny N, Jahani D, Park CB (2017) Characterization of hard-segment crystalline phase of poly(ether- block -amide) (PEBAX ®) thermoplastic elastomers in the presence of supercritical CO₂ and its impact on foams. *Polymer (Guildf)* 114:15–27. <https://doi.org/10.1016/j.polymer.2017.02.088>

34. Standau T, Zhao C, Murillo Castellón S, et al (2019) Chemical Modification and Foam Processing of Polylactide (PLA). *Polymers (Basel)* 11:306. <https://doi.org/10.3390/polym11020306>
35. Zhao D, Wang G, Wang M (2018) Investigation of the effect of foaming process parameters on expanded thermoplastic polyurethane bead foams properties using response surface methodology. *J Appl Polym Sci* 135:46327. <https://doi.org/10.1002/app.46327>
36. Rossacci J, Shivkumar S (2003) Bead fusion in polystyrene foams. *J Mater Sci* 38:201–206. <https://doi.org/10.1023/A:1021180608531>
37. Gibson LJ, Ashby MF (1997) *Cellular Solids*. Cambridge University Press
38. Siviour CR, Jordan JL (2016) High Strain Rate Mechanics of Polymers: A Review. *J Dyn Behav Mater* 2:15–32. <https://doi.org/10.1007/s40870-016-0052-8>
39. Sun Y, Li QM (2018) Dynamic compressive behaviour of cellular materials: A review of phenomenon, mechanism and modelling. *Int J Impact Eng* 112:74–115. <https://doi.org/10.1016/j.ijimpeng.2017.10.006>
40. Andena L, Caimmi F, Leonardi L, et al (2019) Compression of polystyrene and polypropylene foams for energy absorption applications: A combined mechanical and microstructural study. *J Cell Plast* 55:49–72. <https://doi.org/10.1177/0021955X18806794>
41. Beverte I (2004) Deformation of Polypropylene Foam Neopolen® P in Compression. *J Cell Plast* 40:191–204. <https://doi.org/10.1177/0021955X04043718>
42. Ouellet S, Cronin D, Worswick M (2006) Compressive response of polymeric foams under quasi-static, medium and high strain rate conditions. *Polym Test* 25:731–743. <https://doi.org/10.1016/j.polymertesting.2006.05.005>
43. Viot P, Beani F, Lataillade J-L (2005) Polymeric foam behavior under dynamic compressive loading. *J Mater Sci* 40:5829–5837. <https://doi.org/10.1007/s10853-005-4998-5>
44. Viot P, Iordanoff I, Bernard D (2008) Multiscale description of polymeric foam behavior: A new approach based on discrete element modeling. *Polym Sci Ser A* 50:679–689. <https://doi.org/10.1134/S0965545X08060114>
45. Viot P, Maheo L, Mercier A (2011) BEHAVIOUR OF POLYMERIC MULTISCALE FOAM UNDER DYNAMIC LOADING -STUDY OF THE INFLUENCE OF THE DENSITY AND THE WALLS OF BEADS. *Int J Recent Res Appl Stud* 7:

46. Morton DT, Reyes A, Clausen AH, Hopperstad OS (2020) Mechanical response of low density expanded polypropylene foams in compression and tension at different loading rates and temperatures. *Mater Today Commun* 23:100917. <https://doi.org/10.1016/j.mtcomm.2020.100917>
47. Chen Y, Das R, Battley M (2015) Effects of cell size and cell wall thickness variations on the stiffness of closed-cell foams. *Int J Solids Struct* 52:150–164. <https://doi.org/10.1016/j.ijsolstr.2014.09.022>
48. Lee S, Ji W (2020) DVC analysis of a polymer material subjected to tensile loading with synchrotron radiation tomography. *Polym Test* 81:106204. <https://doi.org/10.1016/j.polymertesting.2019.106204>
49. Gillard F, Boardman R, Mavrogordato M, et al (2014) The application of digital volume correlation (DVC) to study the microstructural behaviour of trabecular bone during compression. *J Mech Behav Biomed Mater* 29:480–499. <https://doi.org/10.1016/j.jmbbm.2013.09.014>
50. Bay BK, Smith TS, Fyhrie DP, Saad M (1999) Digital volume correlation: Three-dimensional strain mapping using X-ray tomography. *Exp Mech* 39:217–226. <https://doi.org/10.1007/BF02323555>
51. Buljac A, Jailin C, Mendoza A, et al (2018) Digital Volume Correlation: Review of Progress and Challenges. *Exp Mech* 58:661–708. <https://doi.org/10.1007/s11340-018-0390-7>
52. Mertens JCE, Henderson K, Cordes NL, et al (2017) Analysis of thermal history effects on mechanical anisotropy of 3D-printed polymer matrix composites via in situ X-ray tomography. *J Mater Sci* 52:12185–12206. <https://doi.org/10.1007/s10853-017-1339-4>
53. Kobayashi M, Toda H, Kawai Y, et al (2008) High-density three-dimensional mapping of internal strain by tracking microstructural features. *Acta Mater* 56:2167–2181. <https://doi.org/10.1016/j.actamat.2007.12.058>
54. Hohe J, Hardenacke V, Fascio V, et al (2012) Numerical and experimental design of graded cellular sandwich cores for multi-functional aerospace applications. *Mater Des* 39:20–32. <https://doi.org/10.1016/j.matdes.2012.01.043>
55. Ozturk UE, Anlas G (2011) Finite element analysis of expanded polystyrene foam under multiple compressive loading and unloading. *Mater Des* 32:773–780. <https://doi.org/10.1016/j.matdes.2010.07.025>

56. Ghaffari Mosanenzadeh S, Naguib HE, Park CB, Atalla N (2015) Design and development of novel bio-based functionally graded foams for enhanced acoustic capabilities. *J Mater Sci* 50:1248–1256. <https://doi.org/10.1007/s10853-014-8681-6>
57. Shorten MR (1993) The energetics of running and running shoes. *J Biomech* 26:41–51. [https://doi.org/10.1016/0021-9290\(93\)90078-S](https://doi.org/10.1016/0021-9290(93)90078-S)
58. CHAWLA N, SIDHU R, GANESH V (2006) Three-dimensional visualization and microstructure-based modeling of deformation in particle-reinforced composites. *Acta Mater* 54:1541–1548. <https://doi.org/10.1016/j.actamat.2005.11.027>
59. Williams JJ, Flom Z, Amell AA, et al (2010) Damage evolution in SiC particle reinforced Al alloy matrix composites by X-ray synchrotron tomography. *Acta Mater* 58:6194–6205. <https://doi.org/10.1016/j.actamat.2010.07.039>
60. Kader MA, Islam MA, Saadatfar M, et al (2017) Macro and micro collapse mechanisms of closed-cell aluminium foams during quasi-static compression. *Mater Des* 118:11–21. <https://doi.org/10.1016/j.matdes.2017.01.011>
61. MCDONALD SA, MUMMERY PM, JOHNSON G, WITHERS PJ (2006) Characterization of the three-dimensional structure of a metallic foam during compressive deformation. *J Microsc* 223:150–158. <https://doi.org/10.1111/j.1365-2818.2006.01607.x>
62. Singaravelu ASS, Williams JJ, Goyal HD, et al (2019) 3D Time-Resolved Observations of Fatigue Crack Initiation and Growth from Corrosion Pits in Al 7XXX Alloys Using In Situ Synchrotron X-ray Tomography. *Metall Mater Trans A*. <https://doi.org/10.1007/s11661-019-05519-z>
63. Patterson BM, Henderson K, Smith Z (2013) Measure of morphological and performance properties in polymeric silicone foams by X-ray tomography. *J Mater Sci* 48:1986–1996. <https://doi.org/10.1007/s10853-012-6965-2>
64. Pérez-Tamarit S, Solórzano E, Hilger A, et al (2018) Multi-scale tomographic analysis of polymeric foams: A detailed study of the cellular structure. *Eur Polym J* 109:169–178. <https://doi.org/10.1016/j.eurpolymj.2018.09.047>
65. Patterson BM, Cordes NL, Henderson K, et al (2016) In situ X-ray synchrotron tomographic imaging during the compression of hyper-elastic polymeric materials. *J Mater Sci* 51:171–187. <https://doi.org/10.1007/s10853-015-9355-8>
66. Youssef S, Maire E, Gaertner R (2005) Finite element modelling of the actual structure of cellular materials determined by X-ray tomography. *Acta Mater* 53:719–730. <https://doi.org/10.1016/j.actamat.2004.10.024>

67. Gaitanaros S, Kyriakides S, Kraynik AM (2012) On the crushing response of random open-cell foams. *Int J Solids Struct* 49:2733–2743. <https://doi.org/10.1016/j.ijsolstr.2012.03.003>
68. Singaravelu AS, Williams JJ, Walter J, et al (2019) In situ Four Dimensional (4D) X-ray Microtomography of the Compressive Behavior of eTPU Foam for High Performance Footwear. *Microsc Microanal* 25:364–365. <https://doi.org/10.1017/S1431927619002551>
69. Adams R, Bischof L (1994) Seeded region growing. *IEEE Trans Pattern Anal Mach Intell* 16:641–647. <https://doi.org/10.1109/34.295913>
70. Ghazi A, Berke P, Ehab Moustafa Kamel K, et al (2019) Multiscale computational modelling of closed cell metallic foams with detailed microstructural morphological control. *Int J Eng Sci* 143:92–114. <https://doi.org/10.1016/j.ijengsci.2019.06.012>
71. Hassani A, Habibolahzadeh A, Bafti H (2012) Production of graded aluminum foams via powder space holder technique. *Mater Des* 40:510–515. <https://doi.org/10.1016/j.matdes.2012.04.024>
72. Chen D, Kitipornchai S, Yang J (2018) Dynamic response and energy absorption of functionally graded porous structures. *Mater Des* 140:473–487. <https://doi.org/10.1016/j.matdes.2017.12.019>
73. Johnson KL (1985) *Contact Mechanics*. Cambridge University Press
74. Chen D, Yang J, Kitipornchai S (2015) Elastic buckling and static bending of shear deformable functionally graded porous beam. *Compos Struct* 133:54–61. <https://doi.org/10.1016/j.compstruct.2015.07.052>
75. Amidror I (2002) Scattered data interpolation methods for electronic imaging systems: a survey. *J Electron Imaging* 11:157. <https://doi.org/10.1117/1.1455013>
76. Worobets J, Wannop JW, Tomaras E, Stefanyshyn D (2014) Softer and more resilient running shoe cushioning properties enhance running economy. *Footwear Sci* 6:147–153. <https://doi.org/10.1080/19424280.2014.918184>
77. Sanborn B, Song B (2019) Poisson's ratio of a hyperelastic foam under quasi-static and dynamic loading. *Int J Impact Eng* 123:48–55. <https://doi.org/10.1016/j.ijimpeng.2018.06.001>
78. Soman P, Lee JW, Phadke A, et al (2012) Spatial tuning of negative and positive Poisson's ratio in a multi-layer scaffold. *Acta Biomater* 8:2587–2594. <https://doi.org/10.1016/j.actbio.2012.03.035>

79. Duncan O, Allen T, Foster L, et al (2017) Fabrication, characterisation and modelling of uniform and gradient auxetic foam sheets. *Acta Mater* 126:426–437. <https://doi.org/10.1016/j.actamat.2017.01.004>
80. Rinde JA (1970) Poisson's ratio for rigid plastic foams. *J Appl Polym Sci* 14:1913–1926. <https://doi.org/10.1002/app.1970.070140801>
81. Smith CW, Wootton RJ, Evans KE (1999) Interpretation of experimental data for Poisson's ratio of highly nonlinear materials. *Exp Mech* 39:356–362. <https://doi.org/10.1007/BF02329817>
82. Fortes MA, Teresa Nogueira M (1989) The poisson effect in cork. *Mater Sci Eng A* 122:227–232. [https://doi.org/10.1016/0921-5093\(89\)90634-5](https://doi.org/10.1016/0921-5093(89)90634-5)
83. Widdle RD, Bajaj AK, Davies P (2008) Measurement of the Poisson's ratio of flexible polyurethane foam and its influence on a uniaxial compression model. *Int J Eng Sci* 46:31–49. <https://doi.org/10.1016/j.ijengsci.2007.09.002>
84. Bay BK (2008) Methods and applications of digital volume correlation. *J Strain Anal Eng Des* 43:745–760. <https://doi.org/10.1243/03093247JSA436>
85. Pierron F, McDonald SA, Hollis D, et al (2013) Comparison of the Mechanical Behaviour of Standard and Auxetic Foams by X-ray Computed Tomography and Digital Volume Correlation. *Strain* 49:467–482. <https://doi.org/10.1111/str.12053>
86. Singaravelu ASS, Williams JJ, Ruppert J, et al In Situ X-ray Microtomography of the Compression Behavior of ETPU Bead Foams with a Unique Graded Structure
87. De Carlo F, Albee PB, Chu YS, et al (2002) High-throughput real-time x-ray microtomography at the Advanced Photon Source. In: Bonse U (ed). p 1
88. De Carlo F, Tieman B (2004) High-throughput x-ray microtomography system at the Advanced Photon Source beamline 2-BM. In: Bonse U (ed). p 644
89. Rivers ML (2016) High-speed tomography using pink beam at GeoSoilEnviroCARS. In: Stock SR, Müller B, Wang G (eds). p 99670X
90. Williams JJ, Chapman NC, Jakkali V, et al (2011) Characterization of Damage Evolution in SiC Particle Reinforced Al Alloy Matrix Composites by In-Situ X-Ray Synchrotron Tomography. *Metall Mater Trans A* 42:2999–3005. <https://doi.org/10.1007/s11661-011-0718-8>
91. Gürsoy D, De Carlo F, Xiao X, Jacobsen C (2014) TomoPy: a framework for the analysis of synchrotron tomographic data. *J Synchrotron Radiat* 21:1188–1193. <https://doi.org/10.1107/S1600577514013939>

92. Dowd BA, Campbell GH, Marr RB, et al (1999) <title>Developments in synchrotron x-ray computed microtomography at the National Synchrotron Light Source</title>. In: Bonse U (ed). pp 224–236
93. Münch B, Trtik P, Marone F, Stampanoni M (2009) Stripe and ring artifact removal with combined wavelet—Fourier filtering. *Opt Express* 17:8567. <https://doi.org/10.1364/OE.17.008567>
94. Chen Y, Das R, Battley M (2017) Effects of cell size and cell wall thickness variations on the strength of closed-cell foams. *Int J Eng Sci* 120:220–240. <https://doi.org/10.1016/j.ijengsci.2017.08.006>